On dynamics and thermal radiation of imploding shock waves

by

Malte Kjellander

2010
Technical Reports from
Royal Institute of Technology
KTH Mechanics
SE-100 44 Stockholm, Sweden

Akademisk avhandling som med tillstånd av Kungliga Tekniska Högskolan i Stockholm framlägges till offentlig granskning för avläggande av teknologie licentiatsexamen den 16:e april 2010 i Seminarierrummet S40, Teknikringen 8, Kungliga Tekniska Högskolan, Stockholm.

©Malte Kjellander 2010

Universitetsservice US–AB, Stockholm 2010

On dynamics and thermal radiation of imploding shock waves

Malte Kjellander 2010

KTH Mechanics
SE–100 44 Stockholm, Sweden

Abstract

Converging cylindrical shock waves have been studied experimentally. Numerical calculations based on the Euler equations and analytical comparisons based on the approximate theory of geometrical shock dynamics have been made to complement the study.

Shock waves with circular or polygonal shock front shapes have been created and focused in a shock tube. With initial Mach numbers ranging from 2 to 4, the shock fronts accelerate as they converge. The shocked gas at the centre of convergence attains temperatures high enough to emit radiation which is visible to the human eye. The strength and duration of the light pulse due to shock implosion depends on the medium. In this study, shock waves converging in air and argon have been studied. In the latter case, the implosion light pulse has a duration of roughly 10 μs. This enables non-intrusive spectrometric measurements on the gas conditions.

Circular shock waves are very sensitive to disturbances which deform the shock front, decreasing repeatability. Shocks consisting of plane sides making up a symmetrical polygon have a more stable behaviour during focusing, which provides less run-to-run variance in light strength. The radiation from the gas at the implosion centre has been studied photometrically and spectrometrically. Polygonal shocks were used to provide better repeatability. The full visible spectrum of the light pulse created by a shock wave in argon has been recorded, showing the gas behaving as a blackbody radiator with apparent temperatures up to 6000 K. This value is interpreted as a modest estimation of the temperatures actually achieved at the centre as the light has been collected from an area larger than the bright gas core.

As apparent from experimental data real gas effects must be taken into consideration for calculations at the implosion focal point. Ideal gas numerical and analytical solutions show temperatures and pressures approaching infinity, which is clearly not physical. Real gas effects due to ionisation of the argon atoms have been considered in the numerical work and its effect on the temperature has been calculated.

The propagation of circular and polygonal have also been experimentally studied and compared to the self-similar theory and geometrical shock dynamics, showing good agreement.

Descriptors: Converging shock waves, polygonal shock waves, temperature measurement, argon, plasma creation, ionisation, spectrometry.

Preface

This licentiate thesis in fluid mechanics deals with converging shock waves. Primarily the acceleration of the shock fronts and the radiation from the shocked gas have been studied. The work is mainly experimental and is complemented by numerical calculations and analytical approximations. Part I of the thesis gives an introduction to the field and the experimental equipment as well as a summary of results. Part II consists of 3 papers. In chapter 7 of Part I the respondent's contributions to the individual papers is stated.

March 2010, Stockholm
Malte Kjellander

Part of this work have been presented and accepted for presentation at:

60$^{\text{th}}$ Annual Meeting of the American Physical Society - Division of Fluid Dynamics,
18 – 20 November 2007, *Salt Lake City, Utah, USA*

27$^{\text{th}}$ International Symposium on Shock Waves,
19 – 24 July 2009, *S:t Petersburg, Russia*

Contents

Part I

Overview and summary

CHAPTER 1

Introduction

This work is an experimental and numerical study on converging cylindrical shock waves. Whereas diverging shock waves, such as those created from detonations, are loosing strength as they propagate, focusing shock waves accelerate towards the centre of convergence, where large pressures and temperatures can be achieved.

The first work on converging shock was an analytical treatment by Guderley (1942), while the first experimentally produced converging shock waves were presented by Perry & Kantrowitz (1951). Since then, the ability of converging shock waves to concentrate high amounts of energy at the shock implosion focus has guaranteed continued interest in the field. The most common practical use of shock wave focusing is currently in medicine: extra-corporeal shock wave lithotripsy, which is a method where infinitely weak shock waves are focused on kidney stones inside a patient. The pressure concentration breaks the stones, which can exit the patient the natural way. Stronger shocks can be used for harder matters: creation of high speed jets which in turn can be used for material applications, such as cutting of solids or surface cleaning, or synthesis of diamonds from graphite (Glass & Sharma (1976)).

During the first experiments by Perry and Kantrowitz it was found that the amplification of the converging shocks of initially moderate strength (M=1.5-2) created conditions at the implosion focus such that the gas became radiating. The light emission allows determination of temperature and other gas variables through non-intrusive spectrometric measurements. The present work aims to study the nature of the light emission from converging cylindrical shock waves in argon and to estimate the temperature achieved at the focus. The shock waves are produced in a shock tube designed along similar principles as the tube of Perry and Kantrowitz, with a plane shock wave which is first transformed to an annular shape and subsequently to a cylindrical converging shock. The propagation of the shock is studied and the light pulse created by the shock implosion at the centre of the test chamber is investigated by photometry and spectrometry.

A converging cylindrical shock wave will produce high energy concentrations under the condition that its symmetry is preserved during the convergence process. However, converging circular shocks have been found to be unstable.

Small deviations from a circular shape tend to increase and eventually produce plane portions on the shock front. This leads to a loss of symmetry and a substantial decrease in the focusing effect since various parts of the shock front arrive at different instants and locations in the focal region. Shock waves of polygonal forms have been shown to produce more repeatable results. The spectrometric measurements presented in this work are made on octagonal shock waves for this reason.

CHAPTER 2

Basic equations

This chapter provides a physical and mathematical description of the gas and shock wave jump relations, an introduction to shock wave reflections and shock tube flow, as well as a summary of the research on converging shock waves.

2.1. Theoretical considerations

The gas considered in this chapter is a monatomic gas which, due to the high temperatures and pressure near the centre of convergence, is subject to ionisation. The governing equations of the fluid are the compressible Euler equations but since the gas contains charged ions and electrons, its state equation will differ from that of a fluid-mechanically perfect gas. Consider an inviscid gas with volumetric mass density ρ, temperature T, internal energy e per unit mass and velocity $\mathbf{u} = (u, v, w)$. The basic equations for inviscid compressible flow: conservation of mass, momentum and energy, neglecting body forces and heat addition:

$$\frac{\partial \rho}{\partial t} + \nabla \cdot (\rho \mathbf{u}) = 0 \tag{2.1}$$

The momentum equations, one for each component i:

$$\frac{\partial (\rho u_i)}{\partial t} + \nabla \cdot (\rho u_i \mathbf{u}) = -\nabla p \tag{2.2}$$

The energy equation:

$$\frac{\partial}{\partial t}\left[\rho\left(e + \frac{u^2}{2}\right)\right] + \nabla \cdot \left[\rho\left(e + \frac{u^2}{2}\right)\mathbf{u}\right] = -\nabla \cdot (p\mathbf{u}) \tag{2.3}$$

The equations, here written in conservative form, need to be closed with an equation of state. At low pressures and temperatures, most real gases behave as thermodynamically perfect gases and fulfil:

$$p = \rho R T = nkT \tag{2.4}$$

where R is the specific gas constant, n the number of atoms per unit volume and k the Boltzmann constant. Departures from the perfect state will occur

when the gas is exposed to energetic radiation or attains very high pressures or temperatures[1]. The simple definition of a real gas is one that does not fulfil the perfect gas law. A general equation of state does not exist, which means that different models for different regimes must be used.

2.1.1. *Equation of state of an ionised gas*

Consider a volume V of monatomic gas subjected to high temperatures. As the translational energy of the gas increases, collisions between particles become more frequent and violent. Electrons are excited to higher levels or broken away from their orbits around the nuclei, forming ions and free electrons. During the collisions translational energy is transferred to potential energy in form of excited atoms or ions. The gas now consists of several species: neutral atoms, ions of different charge states and electrons. New variables are needed to describe the gas. The electron number density is denoted as n_e (dimension m^{-3}) and the number density of heavy particles $n_i, i = 0, 1, ..., \ell$ where i is the charge state of the ion and ℓ the atomic number. For the neutral atoms, $i = 0$. The total number density of all heavy particles is denoted $n_H = \sum n_i$, which is equivalent to the original number density n. The degree or number fraction of ionisation is then defined as $\alpha_e = n_e/n_H$. The variable α_e may also be seen as the average number of electrons released by the original atoms. The number fractions of heavy particles in ionisation stage i is defined as $\alpha_i = n_i/n_H$. From the definitions:

$$\sum_{i=0}^{N} \alpha_i = 1 \tag{2.5}$$

Assuming charge conservation, a relation between electron and ion fractions can be found. An ion in stage i has released i free electrons:

$$n_e = \sum_{i=1}^{\ell} i n_i = n_H \sum_{i=1}^{\ell} i\alpha_i = n_H \alpha_e \tag{2.6}$$

$$\alpha_e = \sum_{i=1}^{\ell} i\alpha_i \tag{2.7}$$

The gas consists of a mix of electron and ion gases. Assuming that they individually fulfil perfect gas conditions, the partial pressures from each species are:

[1] Two other cases when Eg. 2.4 is invalid is at extremely low densities, where the gas formulation itself is inapplicable, and at extremely high velocities where relativistic effects come into play.

$$p_e = n_e k T_e \tag{2.8}$$

$$p_i = n_i k T_i, \quad i = 0, 1...\ell \tag{2.9}$$

If the gases are in local thermodynamic equilibrium, which is reasonable for the regimes considered here, they all may be described by a single temperature, $T_e = T_i = T$ (this is however not valid within a shock wave). Using the particle fractions as defined above, the total pressure can then be written as follows, yielding an equation of state for a partially ionised gas:

$$p = p_e + \sum_{i=0}^{\ell} p_i = kT(n_e + \sum_{i=0}^{\ell} n_i) = n_H kT(\alpha_e + 1) \tag{2.10}$$

The specific gas constant of the neutral $n_H m_H$ This can be reformulated using $k = R_A m_A$, where R_A and m_A is the specific gas constant and molecular mass for the atomic gas considered. The weight differences between the ions of different stages are negligible, leading to $\rho \approx m_A n_H$ and:

$$p = \rho RT(1 + \alpha_e) \tag{2.11}$$

2.2. Strong shock wave jump relations

Figure 2.1 illustrates a standing normal shock wave where the pre-shock conditions are known. The pre-shock flow has a Mach number M_1 and the unknown post-shock conditions are sought. For a calorically perfect gas, the post-shock conditions may be solved as functions of M_1 from the conservation equations 2.1-2.3 by considering the shock as a discontinuity. This is a good approximation as long as $M_1 <\sim 5$. For higher Mach numbers the temperature behind the shock starts causing vibrational excitation or chemical reactions. It is no longer possible to find such a simple solution closed-form solution and an iterative method must be used.

Shock jump relations accounting for various combinations of dissociation, radiation or ionisation have been studied extensively, see for example Resler *et al.* (1952), Nieuwenhuijzen *et al.* (1992) or Michaut *et al.* (2004). Here is a short description of the solution procedure for the case when ionisation is considered: for further details, see Zel'dovich & Raizer (2002). A strong shock wave is moving into a gas with known conditions p_1, T_1 etc. The gas in region 1 is in a state such that the ionisation $\alpha_{i1} = [\alpha_1, \alpha_2, ..., \alpha_\ell]_1$ can be considered equal to zero. Considering the system in an inertial frame attached to the shock (Figure 2.1), the flow is steady and the conservation equations can be formulated as following, neglecting internal forces and heat additions:

$$\rho_1 u_1 = \rho_2 u_2 \tag{2.12}$$

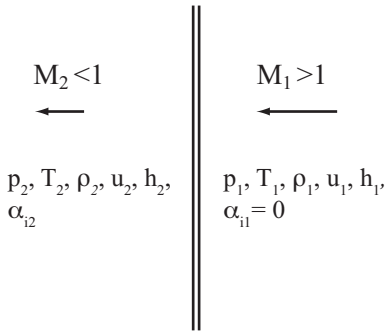

FIGURE 2.1. Normal shock wave. The state (1) before the shock is known.

$$\rho_1 u_1^2 + p_1 = \rho_2 u_2^2 + p_2 \tag{2.13}$$

$$h_1 + \frac{u_1^2}{2} = h_2 + \frac{u_2^2}{2} \tag{2.14}$$

Here the energy is replaced with the enthalpy $h = e + pV$. As described earlier, the ionised gas consists of several species and each particle has a translational energy $\frac{3}{2}kT$. As the gas is ionised, translational energy is transferred to potential energy in the ions. The ionisation potential, denoted I_i, is the energy required to remove an electron from an atom or ion: I_1 is the required energy to remove and electron from a neutral atom, I_2 the energy to remove a second electron from a singly ionised atom, and so on. The total energy required to remove N electrons is therefore $I_{tot} = I_1 + I_2 + ... + I_N$. There also exist electrons excited to higher levels within the ions, whose excitation energy is designated W_i. Summarising, the enthalpy of the ionised gas may be expressed as:

$$h = \frac{5}{2}(1 + \alpha_e)RT + R\sum_{i=1}^{\ell} \alpha_i \sum_{j=1}^{i} \frac{I_j}{k} + R\sum_{i=0}^{\ell} \alpha_i W_i \tag{2.15}$$

To calculate α, local thermodynamic equilibrium is assumed to be established instantaneously and the species distribution is found from the Saha equation, here rewritten using the particle fractions:

$$\frac{\alpha_{i+1}}{\alpha_i} = \frac{1 + \alpha_e}{\alpha_e} \left(\frac{2\pi m_e}{h^2}\right)^{3/2} \frac{(kT)^{5/2}}{p} \frac{2Q_{i+1}^{el}}{Q_i^{el}} \exp\left(-\frac{I_{i+1}}{kT}\right) \tag{2.16}$$

where m_e is the electron mass, h the Planck constant, and $Q_{i+1}^{el}$and Q_i^{el} the internal partition functions of respective species. For a given p and T equation 2.16 can be solved, e.g. by the iterative method of Trayner & Glowacki (1995). More details on the enthalpy and Saha equations may be found in

Appendix B. The system of equations 2.11 and 2.12-2.16 is closed with respect to the unknowns, but an iterative method is necessary to find the post-shock conditions:

1. An initial value of ρ_1/ρ_2 is estimated, based on e.g. the standard Rankine-Hugoniot equations.
2. New values of p_2, u_2 and h_2 are calculated using Eq:s 2.12-2.14.
3. With the new values, a temperature which simultaneously fulfils the enthalpy according to Eq. 2.15 and the equilibrium conditions according to Eq. 2.16 is sought using a bi-secant method.
4. A new ρ_1/ρ_2 can now be found from the equation of state 2.11, which is used as a new guess in step 1, until the error between the resulting and initial value is as small as acceptable or machine allows.

Figure 2.2 shows the equilibrium conditions behind a normal shock wave in argon with initial temperature $T = 293$ K and three different initial pressures $p_1 = 0.1$, 0.01 and 0.001 atm. The dashed lines are the Rankine-Hugoniot relations for a perfect gas without ionisation depending only on Mach number. The ionisation has a strongly limiting effect on the temperature as energy is transferred from translational to potential energy. Whereas the compression approaches an asymptotic value ($\rho_2/\rho_1 = 4$ for $\gamma = 5/3$) for the constant-composition gas this is not the case for the ionising shock. The peak corresponds to the maximum of the first ionisation stage, whereafter the translational energy increases relative to the potential energy, resulting in a decrease of density.

2.3. Shock tube flow

Shock tubes are devices used primarily to study high temperature gases. A simple shock tube is a long tube, usually with a rectangular or circular cross section, consisting of two sections separated by a thin membrane. The first is called the driver section and is filled with a gas at high pressure. The other, low pressure section is called the driven section. A shock tube at initial conditions is sketched in Figure 2.3.

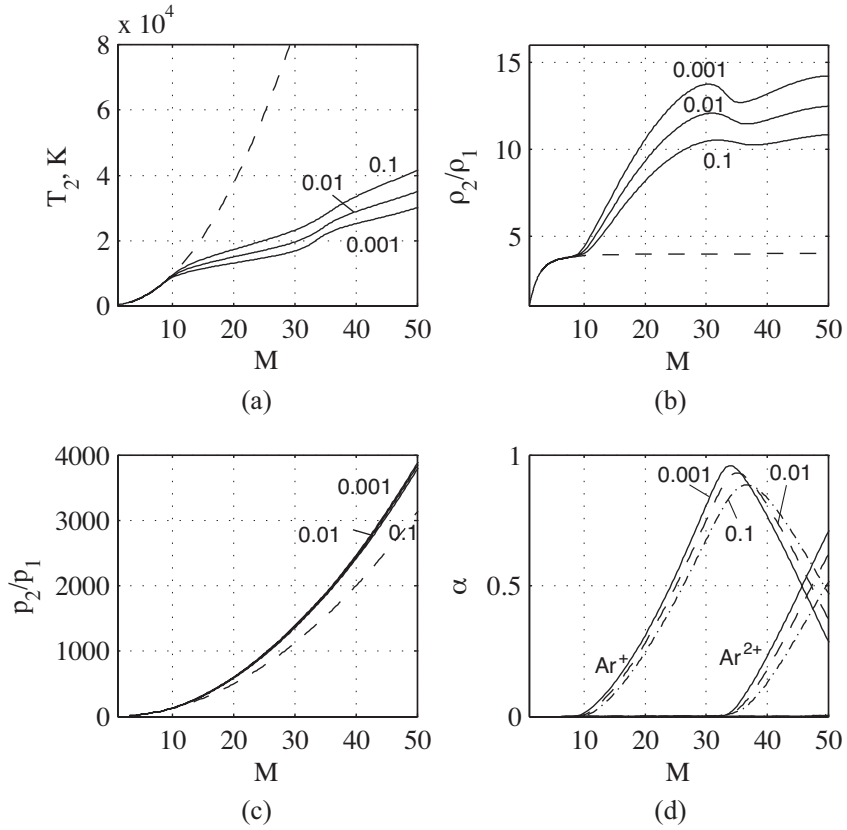

FIGURE 2.2. Effect of ionisation on shock jump conditions (a-c) at three different initial pressures $p_1 = 0.1$, 0.01 and 0.001 atm. Dashed lines represent the non-reacting Rankine-Hugoniot solution. The ionisation is presented in (d).

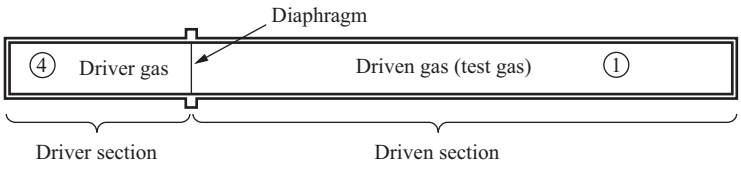

FIGURE 2.3. Shock tube before membrane burst. Region 4 and 1 is the initial gas states.

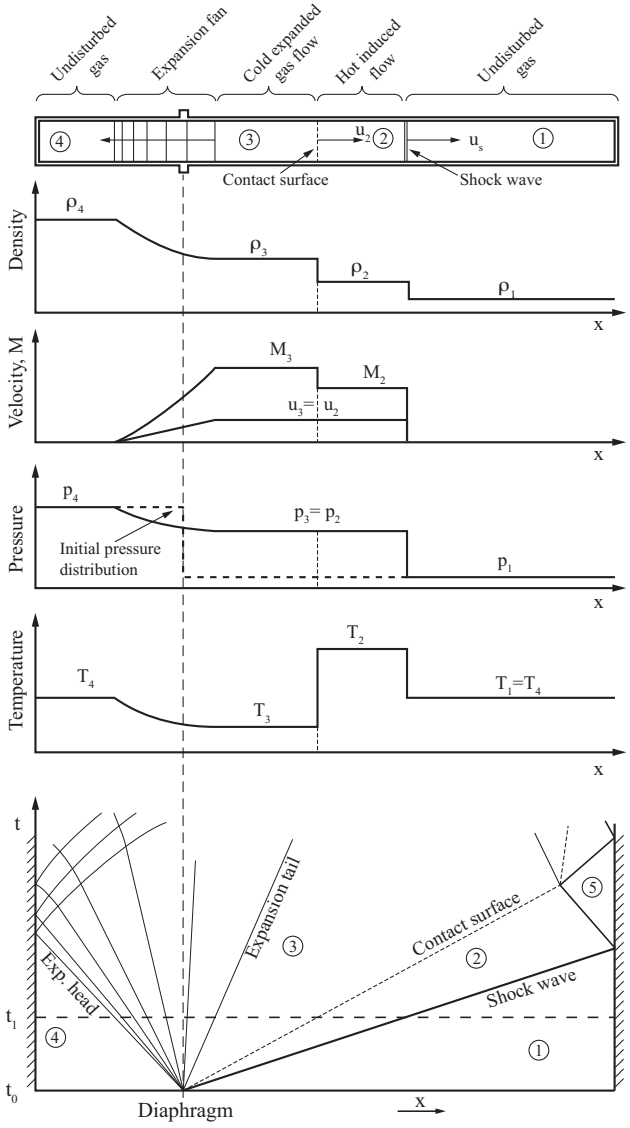

FIGURE 2.4. Shock tube flow at time t_1. The density, velocity, pressure and temperature distribution at time t_1. The x-t diagram (bottom) shows the propagation of the shock front, contact surface and expansion fan. The horizontal dashed line shows the time instant corresponding to the graphs above.

When the separating membrane bursts, pressure waves start propagating into the low pressure gas. The speed of sound behind the successive waves increases, resulting in a compression of the waves into a shock wave moving downstream at a velocity u_s. Figure 2.4 shows the flow and gas conditions in a shock tube at a time $t = t_1$ and an x-t propagation diagram. The instant t_1 corresponding to the graphs is shown as a horizontal dashed line in the x-t diagram. The shock wave pulls the gas it passes through with it, inducing a hot flow with a velocity u_2. This is the flow (region 2) which is often used for studying high temperature gases or used for hypersonic aerodynamic testing in a shock or expansion tunnel. The gas in region 3 is the gas originally in the high pressure section propagates at the same velocity u_2 as the induced flow. The surface between the gases is called the contact discontinuity, which in reality is a turbulent region filled with a mixture of both gases developed during the diaphragm burst and not as sharp as the name or the presentation in Figure 2.4 would suggest. The entropy and temperature changes over the surface, but the pressure and velocity are constant.

Simultaneously with the compression wave, an expansion wave starts moving upstream (left in the figures) at the diaphragm burst. The expansion tail is moving upstream at the local speed of sound, but since the gas at that point is moving downstream at velocity u_2, the tail may be moving either left or right in the laboratory frame, depending on whether u_2 is sub- or supersonic. In Figure 2.4 the tail is depicted moving right/downstream, indicating a supersonic u_2. In region 5, the shock wave has reflected on the farther wall and travelled back into the shock-induced flow, further increasing the pressure and temperature.

The flow field presented in the x-t diagram can be completely determined from the initial conditions in regions 1 and 4 with the ideal assumptions of inviscid flow and discontinuous shock and contact surface. The resulting Mach number of the shock wave $M_s = u_s/a_1$ depends on the initial ratios of the pressures p_1 and p_4 and the speeds of sound a_1 and a_4 in the high and low pressure gas. A one-dimensional treatment is presented in Resler *et al.* (1952); the result is reproduced in equation 2.17 and 2.18. The first equation gives the relation between the initial pressures, speeds of sound and shock Mach number while the second equation shows the maximum theoretically achievable shock Mach number M_{max}. Apparently, even though higher pressure ratios strengthens the shock wave, the speed of sound ratio sets a limit on the shock wave strength. The equations are derived on the assumption of constant heat capacity and neglecting viscosity. More information on the theory of shock tube flow may be found in Anderson (2003) or, concerning deviations from the ideal assumptions, Emrich & Wheeler (1958).

$$\frac{p_4}{p_1} = \left[\frac{2\gamma_1 M_1^2 - (\gamma_1 - 1)}{\gamma_1 + 1}\right]\left[\frac{a_4}{a_4 - \frac{1}{2}(\gamma_4 - 1)u_2}\right]^{\frac{2\gamma_4}{\gamma_4 - 1}} \tag{2.17}$$

$$M_{max} = \frac{\gamma_1 + 1}{\gamma_4 - 1} \frac{a_4}{a_1} \tag{2.18}$$

2.4. Pseudo-steady shock reflections

The interactions between several shock waves or between shocks and solid boundaries are important in this work, so a brief introduction will be given here. The reflection pattern appearing when a shock wave collides with an inclined solid surface is dependent on the inclination θ and Mach number M_s of the wave. The different patterns are categorised in two main groups, *regular* and *irregular* reflections. Irregular reflection includes von Neumann reflection and different forms of Mach reflections. The categorisation and transition criteria are still discussed and studied. This introduction is primarily based on Ben-Dor (2007).

Figure 2.5 illustrates some of the possible shock reflection patterns. A plane shock wave i is moving perpendicularly along a surface from left to right, with velocity u_s and Mach number M_s. The shock propagates into a gas at rest. At a certain point it strikes an inclination with angle θ. If θ is large enough, regular reflection occurs, Fig. 2.5 (a), where the reflected shock r is connected to the incident shock at the surface (point P). Although the shock waves are not stationary in the laboratory frame, the flow is steady in a reference frame attached to point P and the systems are referred to as pseudo-steady.

Irregular reflections occur when the angle θ is so small that a physical flow can not be established by the regular reflection pattern (a). Two different Mach reflections are shown in (b) and (c). A shock wave m normal to the surface appears - called a Mach stem after its first observer - inducing a parallel flow close to the surface. The incident and reflected shock wave instead meet together with the stem at a point away from the wall, called the triple point (T). A slip line divides the gas that has passed the incident and reflected shock from the gas affected by the stem. If the flow immediately behind the triple point between r and s is supersonic relative to T, the near part of the reflected wave becomes straight. This pattern is designated as a transitional Mach reflection (c). A von Neumann reflection is a weaker form of irregular reflection, where the reflected shock r is a compression wave. Other types exist, but this text is limited to stating their existence: stationary and inverse Mach reflections and double and triple Mach reflections.

For small angles θ, no reflection is possible and the shock segment closest to the surface curves and becomes normal to the wall. Except in the already cited source, further reading may be found in Hornung (1986), Ben-Dor & Takayama (1992).

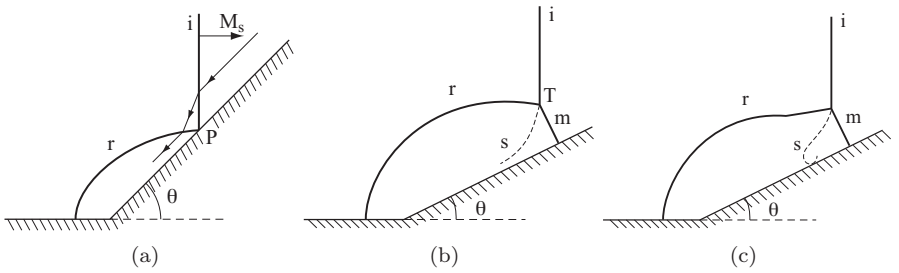

FIGURE 2.5. A few shock reflection types: (a) regular reflection; (b) single Mach reflection; (c) transitional Mach reflection. The streamlines in figure (a) are presented as seen from a frame of reference attached to the intersection point P.

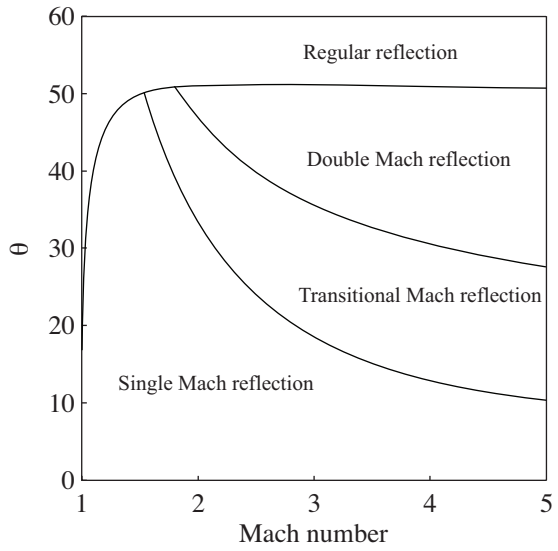

FIGURE 2.6. Approximate reflection regimes for shock waves in air (γ=1.4).

2.5. Previous work on converging shock waves

This section gives a short summary of the study of converging shock waves, starting in the 1940s. The theoretical approach consists mainly of self-similarity studies and approximate methods, such as geometrical shock dynamics. The focus in this chapter is however on experimental work.

2.5.1. *Theoretical studies*

The first analytical treatment of converging shock waves was made by Guderley (1942), who derived a self-similar solution for shock waves of cylindrical or spherical form. He found the following expression for the time t and radius r of an initially strong shock wave converging in an inviscid, perfect gas:

$$\frac{r}{r_0} = \left(1 - \frac{t}{t_0}\right)^a \tag{2.19}$$

where r_0 and t_0 is the initial radius and time of focusing. The self-similar exponent a depends on geometry and the medium through which the shock is propagating. Analyses of the self-similar problem and derivations of self-similar exponents with an ever increasing number of significant digits have since been made in a number of studies, e.g. Butler (1954), Stanyukovich (1960) , Fujimoto & Mishkin (1978) and Ponchaut *et al.* (2006). Table 2.5.1 shows the history of the exponent for cylindrical and spherical shock waves for $\gamma = 1.4$ and $\gamma = 5/3$. The assumption of an initially strong shock was removed by Ponchaut *et al.* (2006), who showed that solutions also exist for infinitesimally weak shocks.

The deviating value of Fujimoto & Mishkin (1978) comes from their claim that the problem might be solved in closed form, although other authors (Lazarus (1980),Van Dyke & Guttman (1982)) have challenged this. A numerical integration of the shock wave was carried out by de Neef & Hechtman (1978), which agreed well with the previous analytical work. Chisnell (1998) made an approximate analytical determination of the exponent agreeing very well with those acquired from the exact form. His solution also gave a description of the flow field at all points behind the converging shock front.

Nakamura (1983) used the method of characteristics to solve the problem and acquired exponents agreeing well with the self-similar solution.

Approximate methods neglecting the influence of the flow behind the shock wave were developed independently by Chester (1954), Chisnell (1955) and Whitham (1958). It is a geometrical approach based on tracking the shock fronts along rays perpendicular to the fronts, analogous to acoustic wave theory. The approach, by some authors called CCW-methods after the listed authors, by other geometrical or Whitham shock dynamics (GSD), has proved to be a good approximation and agrees well with the Guderley similarity solution. The theory has been expanded by Whitham to allow uniform flow in front of the shock and by Apazidis *et al.* (2002) to also account for shocks propagating into non-uniform flows.

A comparison of the solutions of self-similar theory, geometric shock dynamics as well that of a numerical Euler solver was presented by Hornung *et al.* (2008), showing good agreement.

TABLE 1. Guderley's self-similar exponent. Significant digits and error margins reproduced from sources. M_s is the initial shock strength during the experiments.

	Cylindrical $\gamma = 7/5$	Cylindrical $\gamma = 5/3$	Spherical $\gamma = 7/5$	Spherical $\gamma = 5/3$
Guderley (1942)	0.834	-	0.717	-
Butler (1954)	0.835217	-	0.717173	0.688377
Stanyukovich (1960)	0.834	-	0.717	-
Welsh (1967)	0.835323	0.815625	0.717174	0.688377
Lazarus & Richtmyer (1977)	0.83532320	0.81562490	0.71717450	0.68837682
Fujimoto & Mishkin (1978)	-	-	0.707	0.687
Mishkin & Fujimoto (1978)	0.828	0.814	-	-
de Neef & Hechtman (1978)	0.835 ± 0.003	-	-	-
Van Dyke & Guttman (1982)	0.835324	-	0.7171745	0.6883768
Nakamura (1983)	0.8342/0.8345	-	0.7173	-
Hafner (1988)	0.835323191952911	0.815624901431225	0.717174501488999	0.688376822922543
Chisnell (1998)	0.83532	0.81562	0.71716	0.68837
Ponchaut *et al.* (2006)	0.835323191953	0.8156229691667	0.717174501488	0.6883740859496
Experiments:				
Kleine (1985)	$0.832(+0.028, -0.043)$	$M_s = 1.3 - 2.1$		
Takayama *et al.*(1987)	0.831 ± 0.002	$M_s = 1.1 - 2.1$		
Hosseini & Takayama (2005)			0.738	

2.5.2. *Experiments*

The first experiments on converging shock waves were carried out by Perry & Kantrowitz (1951). Using a shock tube with an inner body shaped as a teardrop, they produced circular cylindrical shock waves which were studied with schlieren optics. They found that the shock waves managed to concentrate enough energy to make the gas at the centre of implosion emit light - even more so when argon was used as a test medium. The production of light was believed to be caused by ionised gas and taken as an indicator of high pressures and temperatures. Two different initial Mach numbers were studied, 1.4 and 1.8. They concluded that creating symmetric cylindrical shocks was more difficult with the higher Mach number, due to instability of stronger shocks. Since then several experimental studies have been conducted, in modified shock tubes or other specifically designed devices.

2.5.2a. *Spectroscopic measurements.* Knystautas *et al.* (1969) made experiments with converging detonation waves in a cylindrical chamber filled with an acetylene-oxygen gas at an initial pressure of 120 Torr. They measured the intensity of the luminescent centre at two wavelengths and compared to a blackbody radiator, estimating a maximum temperature of 189,000 K.

Roberts & Glass (1971) measured the emission from converging shock waves in a hemispherical chamber filled with a oxygen-hydrogen gas at high pressures (6.8-27.2 atm). The shock waves were generated with an exploding wire in the center of the chamber. The radiation was continuos with a blackbody temperature of ∼5000 K. They also stated that the temperature reported by Knystautas *et al* was estimated too high due to erroneous use of Wien's law. The work was continued by Roig & Glass (1977), who presented time resolved blackbody temperatures from measurements on six wavelength regions, with similar peak temperatures (4500-6000 K).

Saito & Glass (1982) made spectrometric temperature measurements on shock waves in a hydrogen-oxygen mixture. Shock waves were initiated by exploding wire at the centre of a hemispherical implosion chamber and allowed to reflect and converge. They also used explosives attached directly at the walls. Time-resolved recordings on the radiation intensity was made at eight wavelengths in the visible region. The emission was found to be continuos and comparisons with the blackbody function yielded temperatures in the range 10,000-13,000 K for gas runs and 15,000-17,000 K for the explosive runs.

Matsuo *et al.* (1985) conducted spectrometric measurements on converging shock waves in air. Strong shock waves were created by detonation at the centre of a test circular chamber, which reflected at the walls and focused. The light emission at the focus was measured and compared to the blackbody function. Time-resolved intensity was measured with photomultiplier tubes at a number of separate wavelengths between 400 and 500 nm and temperatures in the range of 13,000-34,000 K.

2.5.2b. *Measurements on stability and flow propagation.* Neemeh & Ahmad (1986) studied the stability of cylindrical shock waves, experimentally and theoretically. Perturbations were introduced externally, by placing cylindrical rods in the path of the shocks. They made a number of conclusions: the region of collapse was shifted due to the disturbance and depending on whether the shock was strong or weak, the shift was either on the disturbed side of the centre or beyond. Perturbations were found to grow exponentially, in good agreement with Butler's (already cited) theoretical work, indicating that cylindrical shocks are unstable.

Takayama, Kleine & Grönig investigated the stability of converging circular cylindrical shock waves. The experiments were conducted in two different shock tubes - one at the Stosswellenlabor, RWTH in Aachen and one at the Institute of High Speed Mechanics, Tohoku University in Sendai - with similar basic designs as that of Perry and Kantrowitz: a circular tube with a conical inner body. It was concluded that the shock waves were always unstable in these tubes. The results showed that the appearance of the instabilities are very sensitive to the design of the supports of the inner body. One tube had three supporting struts and the other four. In the tube with three struts the deformations became triangular, while square deformations appeared in the second tube. The deformations were designated as three- and four-mode instabilities. Takayama and Kleine also achieved experimental values for the self-similarity exponent, which agreed well with theory (see Table 2.5.1). Watanabe & Takayama (1991) continued stability experiments in the Sendai tube and concluded that small perturbations were amplified during convergence resulting in the formation of triple points.

Further stability analyses were made by Watanabe *et al.* (1995), who built a vertical shock tube without supports for the inner body to eliminate such disturbances. The resulting shocks did keep their circular form better than in shock tubes with supports. Deformation of the shock shape still occurred however, and reason for this was believed to be small changes in area between the inner and outer body of the coaxial channel. Also in this experiment cylindrical rods were placed in the test section to introduce corresponding disturbances in a controlled way. One conclusion was that when several modes were combined, the lowest dominated the others.

Hosseini & Takayama (2005) constructed a hemispherical chamber for focusing of shock waves created by explosives. The final Mach number of the converging shock was between 2.5 and 8. They created a transparent chamber with aspheric outer surface in order to use holographic interferometry. They made high-speed video recordings of the shock wave propagation and discussed the effect different methods to initiate the shock had on the stability.

Although some authors have argued that converging circular cylindrical shock waves are stable (Lee & Knystautas (1971)) most have claimed the opposite, which indicates that loss of symmetry sets the limit for the ability of energy concentration. Whitham (1973) used his ray-shock theory to show that circular shocks indeed are unstable. Henshaw *et al.* (1986) developed a numerical scheme based on Whitham's theory, which Schwendeman & Whitham (1987) applied the theory to polygonal shock waves. He found that a symmetric polygonal shock is dynamically stable in the sense that the shock front will undergo a periodic transformation between n and 2n sided polygonal form while retaining the symmetry of the shock structure. Apazidis & Lesser (1996) made a theoretical study using geometrical shock dynamics to design a chamber in which such shapes could be created.

2.5.3. *Previous work at KTH Mechanics*

Experiments on converging shock wave were initiated at KTH Fluids Physics Laboratory in 1996. Based on the calculations by Apazidis & Lesser (1996) with modified geometrical shock dynamics, polygonal shock waves with sharp corners were generated in a confined cylindrical chamber with smooth exchangeable boundaries (Johansson *et al.* (1999), Apazidis *et al.* (2002)). A shock wave was generated in the centre of the chamber by electric discharge or exploding wire. The shock wave diverged, reflected on the smooth polygonal boundary and converged. Schlieren photography was used for visualisation. The experimental results agreed well with the modified geometrical shock dynamics for shocks moving into a non-uniform flow. More information can be found in the licentiate thesis by Johansson (2000).

However, the method of initiating the shock in the chamber created a disturbance zone in the centre. To avoid these disturbances a horizontal shock tube was constructed. The tube works on similar principles as that of Perry & Kantrowitz (1951) and Takayama *et al.* (1987) and is described in Chapter 3. The shock tube has exchangeable reflector boundaries akin to those used in the confined chamber. Polygonal shocks with different number of sides were generated in the tube and studied with schlieren optics (Eliasson *et al.* (2006)). The four-mode instability reported by Takayama *et al.* (1987) was observed in the KTH tube as well. Another way of reshaping the shocks was employed: small cylinders were inserted in the tube to deform the shocks into polygonal shapes (Eliasson *et al.* (2007*a*)). The behaviour of polygonal shocks rearranging themselves in periods was observed and showed good qualitative agreement with the calculations of Schwendeman & Whitham (1987) and Apazidis & Lesser (1996). The light production was also studied photometrically (Eliasson *et al.* (2007*b*)). The total intensity of the light pulse was measured for polygonal and circular shock shapes. It was shown that the light intensity between different shock tube runs were more consistent when the shocks had polygonal shapes, albeit not as strong. This is an indication that polygonal shocks are more stable.

The experiments were coupled with numerical calculation based on the Euler equations, including a numerical determination of the self-similarity exponent which agreed well with analytical data. For further information, see the doctoral thesis by Eliasson (2007).

CHAPTER 3

Experimental methods

The experiments were performed at the shock tube facility of the *Fluid Physics Laboratory* at *KTH Mechanics*. The facility consists of a shock tube with circular cross section, designed to create converging cylindrical shock waves, and equipment for detection and measurements of the propagation and light production of the converging shock waves. This chapter aims to describe the setup used in the experiments presented here and to work as an introduction to future users of the facility.

3.1. Experimental apparatus

3.2. Shock tube

The cylindrical shock tube is illustrated in Figure 3.1. The capital letters designates the different parts of the tube: (A) is the driver section and (B)-(E) the driven section. The diaphragm is located at the intersection of parts (A) and (B). The driven section consists of a inlet tube (B), an annular section (D) and a cylindrical test section (E). The purpose of the inlet tube is to allow the shock wave to attain a plane shape before entering the annular section. A transformation section (C) consisting of a coaxially aligned conical inner body which transforms the shock wave into an annular shape. The geometry is designed to keep the total area of the shock front constant through the transformation phase as well as in the annular channel. The height of the channel is 10 mm. The annular channel ends into an open chamber with a sharp 90° bend. The test section is made up of this open chamber. The shock wave reflects against the end wall, creating a high pressure and temperature region building a piston-like compression towards the test section which has a width (channel height) of 5 mm. The interactions at the bend are complex, resulting in a shock wave moving with increasing speed towards the centre of the cylindrical test section. The principal propagation of the shock wave is sketched in Figure 3.2. The test section consists of the central part of the chamber which is framed on both sides by glass windows for easy visualisation. The observation window (W_2) is a 15 mm thick borosilicate glass (Borofloat 33) disc with good thermal resistance and full optical transmission down to the UV range.

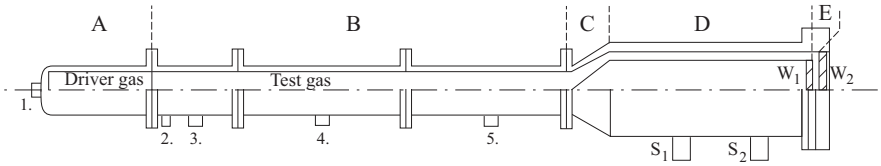

FIGURE 3.1. Schematic drawing of the shock tube. The principal sections are: A driver section; B inlet tube; C transformation section; D annular channel and E test section. Shock sensors S_1 and S_2, and glass windows framing the test section W_1 and W_2. Connections to the tube 1-5, present use: 1, high pressure sensor; 2, burst indicator; 3, low pressure sensor; 4, test gas valve; 5 vacuum pump.

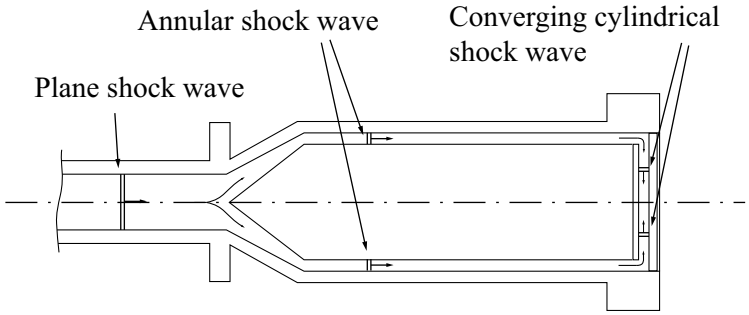

FIGURE 3.2. Schematic drawing of the shock wave propagation through the tube. The plane shock enters the transformation section from the inlet tube, becomes annular before going through the bend into the cylindrical test section. The part of the shock wave that reflects on the test section wall and returns down the annular channel is omitted for clarity.

The low pressure section is evacuated by a two-stage vacuum pump connected to the tube at (5). Test gas can be admitted into the tube via the valve at (4). When argon is used as test gas, the process of filling the tube begins by evacuating the tube maximally, filling it with gas to the desired test pressure, whereupon the evacuation and refilling process is repeated once more. The argon gas used in the present experiments had a purity rate of 99.99%, according to the manufacturer. After the evacuation the gas is allowed to retain room temperature, a process which takes about two minutes.

Regular air or commercial helium is used as driver gas. Thin aluminium diaphragms separates the sections (A) and (B). Located behind the diaphragm

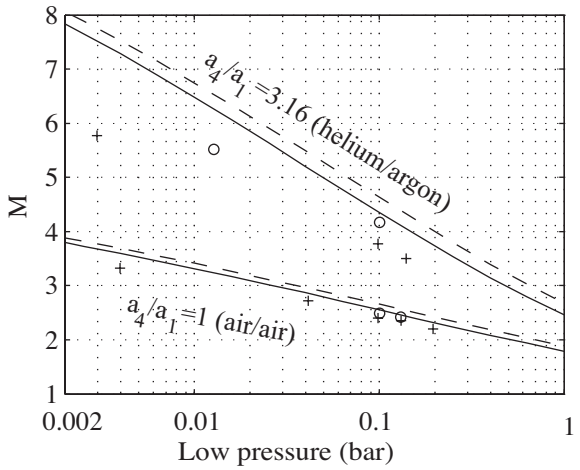

FIGURE 3.3. Guide to achievable Mach numbers with membranes thickness of 0.5 mm (+) and 0.7 mm (o) for two gas combinations. Theoretical values have been added for comparison (0.5 mm: full lines, 0.7 mm: dashed lines). Upper curves have helium as driver and argon as test gas, while the lower have air as both gases.

is a cross-shaped knife. The knife has a twofold purpose: to ensure ruptures at set pressure differences and to ensure consistency in the mechanical opening process. The pressure difference required to force the diaphragm towards the knife is determined by the thickness and strength of the membrane, which assures that rupture occurs at the same pressure difference each run. In this work membranes of thickness 0.5 mm and 0.7 mm were used. The rupture pressure difference is 1.65±0.05 MPa for the thin membranes and 2.3±0.1 MPa for the thick. The pressures and variance of pressures between runs are slightly dependent on the handling of the filling of the gas and do vary considerably from the stated values. If care is taken to fill the tube in the same manner each shock tube run, the variance between shots can be decreased to as low as 10 kPa.

The pressure in both sections is measured with a pressure transducer and indicator (GE Druck DPI 150), connected to the high pressure section at 1 (see Figure 3.1) and to the low pressure section at (3). An external module (GE Druck IDOS) connected to the indicator is used to measure the high pressure. The highest pressure at the moment of membrane rupture is recorded and used as the value for the high pressure p_4.

The shock speed is measured in the annular tube by two temperature sensors, called "shock sensors" in this text. These are inserted flush with the

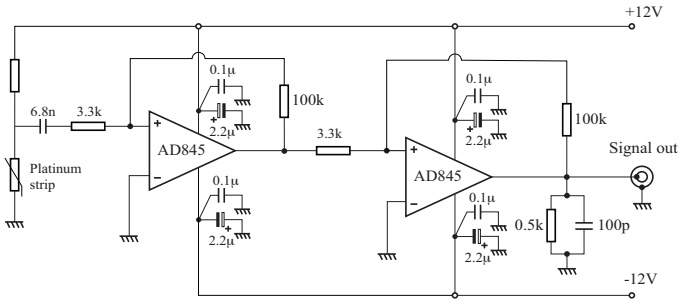

FIGURE 3.4. Circuit diagram of shock sensor amplifier.

outer wall of the channel and separated by 25.0 cm. Each consists of a strip of platinum film painted on the tip of a glass cylinder with a diameter of 10 mm inserted through the tube wall and aligned flush with the inner surface of the outer wall of the annular channel. The platinum strip is connected to a fast amplifier and the circuit diagram is shown in figure 3.4 (Eliasson (2007)). Figure 3.3 shows measured Mach numbers for membrane thickness of 0.5 mm and 0.7 mm, compared with the theoretical Mach number after membrane rupture according to equation 2.17. The figure is intended as a guide to what shock strengths can be achieved with the membranes at which low pressures. The Mach numbers are measured in the annular channel. The shocks have passed the conical transformation section which leads to reflections and dissipative losses, whereas the theoretical values show the ideal case in a plane tube.

3.3. Triggering and Synchronisation

Capturing images or spectra of a very rapid phenomenon craves an accurate triggering system to control the exposure of the cameras. Several trigging methods have been used: the shock sensors, a trigger system making use of a laser beam deflected by the shock wave and the photo-multiplier tube. A time diagram (to scale) of the flow is shown in Figure 3.5.

3.3.1. *Shock sensors*

The temperature sensors positioned on the outer surface of the annular tube may be used for triggering. It is a robust system and apt for all trigging purposes except when rapid events very close to the focal region are studied, when a more precise system is necessary. Either the first or second sensor may be used, depending on circumstances. Typically, the signal output is connected to a time delay unit (DG525, Stanford Research Systems), which in turn triggers the laser, camera, oscilloscope or spectrometer.

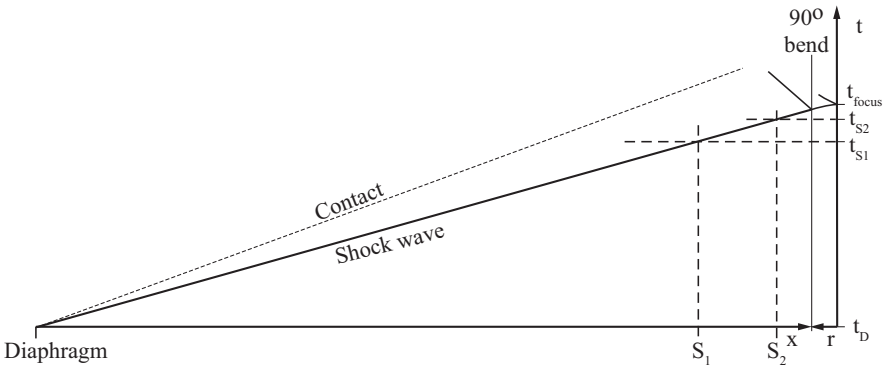

FIGURE 3.5. Idealised time diagram of shock propagation in the annular shock tube. The flow is presented on a single axis and omits the complex structures created at the 90° bend, where x is the length coordinate in the horisontal part and r the radius of the test section. The expansion fan and anything originating upstream of the diaphragm is omitted.

3.3.2. *Laser triggering*

The signal from the downstream shock sensor may be used for triggering, but since it is positioned far from the centre of the test section it is not precise enough for measurements requiring a timing accuracy on the order of 100 ns. The shock wave needs, depending on strength, a time of the order of 200-300 μs to propagate from the shock sensor to the focus. The time variation between shots amounts to several microseconds. A non-intrusive method was therefore developed to detect the shock closer to the focus. A continuos laser beam is directed through the test section, about 15 mm from the centre. Deflections of the laser beam caused by the passing shock wave are detected by a fast photodiode. The angle of the laser varied between experiments, depending on the other measurement equipment placed in front of the test section.

Figure (3.6) shows a photograph and a principal sketch of the setup. A HeNe laser beam is directed through the test section at a small angle, passes through both glass windows and is reflected back by a mirror inside the inner body. The beam path is in the horizontal plane lying on the tube centreline. The beam exits the test section on the opposite side of the centre. A lens (f=+80 cm) focuses the beam on an optical fibre, which leads the light to a fast photodiode (Hamamatsu S5973). The circuit that amplifies the photodiode current is given in figure 3.7. It consists of a primary current amplifier with very fast response and a secondary amplifier to increase the output voltage to the trigging levels of the time delay unit. Characteristics were determined with

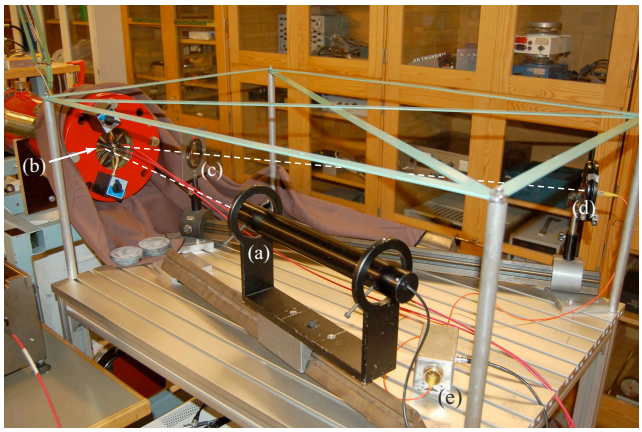

(a)

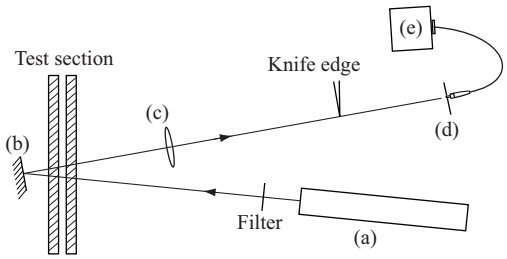

(b)

FIGURE 3.6. Photograph and sketch of the laser triggering setup. Description for both: (a) HeNe laser; (b) mirror (inside tube); (c) 80 mm lens, focusing the laser beam on (d) optical fibre mounted in a traverse; (e) photodiode and amplifier. Path of laser beam sketched on photo. Two fibres collecting light from the implosion to the photo-multiplier tube and spectrometer (lower left corner) can also be seen in the photo. A damping filter and a knife edge may be used additionally.

a pulse laser: the rise time of the primary amplifier is about 20 ns and the rise time of the combined circuit including the secondary amplifier is 100 ns.

The response to a passing shock wave consists of four peaks: the first two correspond to the converging shock wave passing the laser beam going into and out from the test section respectively, while the second pair corresponds to the outgoing reflected shock wave. The peaks have a certain slope depending on the angle of the laser beam. For triggering, the photodiode signal is set to the trigger input of the delay unit. The system is very sensitive to the position

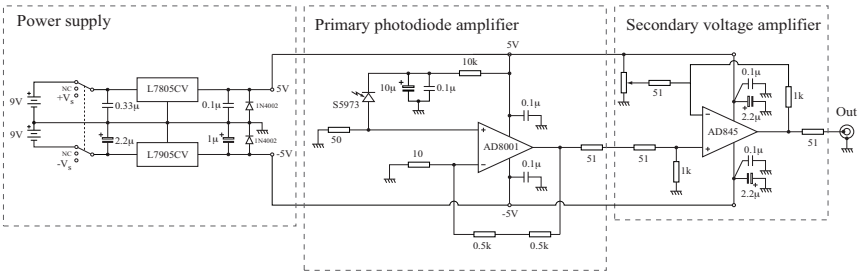

FIGURE 3.7. Circuit diagram of the photodiode amplifier. V_s may be set to $5 - 15$ V.

of the receiving optical fibre. The fibre is placed on a traversing system and before each shot it is moved to its most sensitive position where it generates the maximum signal. The triggering level on the DG535 is set to just below the value of the maximum: when the shock passes the generated signal drops.

3.3.3. *Photo-multiplier signal*

A simple way to trigger the spectrometer is to use the photomultiplier tube detecting the light created by the shock wave itself. It is particularly useful for measuring the light spectrum after shock focusing, during the relaxation phase of the gas in the centre, but the small rise in emission just prior to the collapse enables this method to be used to detect the beginning of the implosion pulse as well. The problem that arises in the latter case is that this initial light increase is relatively slow, not completely repeatable and, above all, very close to the implosion peak itself.

3.3.4. *Burst indicator*

Immediately downstream of the membrane in the driven section, an electric conductor runs through the tube wall (2) in Figure 3.1. The conductor is electrically insulated from the metal tube and the conductor terminal is aligned flush with the inner side of the tube. When the membrane bursts it hits the conductor tip, connecting it with the tube. The change in potential may be used as an indicator for the membrane burst event or as a trigger.

3.3.5. *Pressure comparator*

A circuit used for triggering the Nikon camera was built. It monitors the pressure in the driver section and triggers an infrared remote control (a modified Nikon ML-L3) to turn on the camera once a certain pressure is reached. A pressure transducer (Keller Series 21R) was connected on a T-joint inserted on the tube between the Druck pressure indicator and the driver section. The sensor signal is connected to a comparator circuit (see Figure 3.8), which toggles

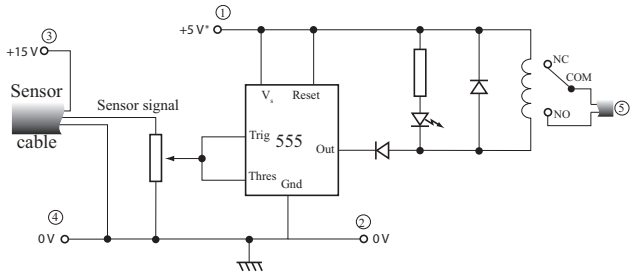

FIGURE 3.8. Circuit diagram of pressure comparator. Connectors (1) and (2): power supply for comparator, (3) and (4): power supply for pressure transducer . Output cable to IR remote (5).

a relay when the pressure signal exceeds 2/3 of the comparator supply voltage. A potentiometer is used to set the triggering pressure and a LED indicates when the relay is activated. The circuit short cuts the two conductors in the output cable to the infrared remote which triggers the camera.

3.4. Flow visualisation: Schlieren optics

Flow visualisation is provided with schlieren optics. A schlieren system makes use of the density-dependence of the refractive index of light. Here follows a short introduction and description of the present setup. Three main components are necessary: a collimated light source, a light blocker - called a schlieren stop - and a camera. The principle is simple: the parallel light rays illuminate the test section of interest and are afterwards focused on the stop, which partially or completely blocks the light. Density gradients in the test section make the parallel rays deflect. Light that would otherwise have been blocked by the stop will now pass it (or vice versa - light that would have passed may instead be blocked). The density changes will thereby appear as darker or brighter areas on the image plane after the schlieren stop. A camera takes photographs of the image plane.

Two principal optical setups were used. One that had all optical elements arranged on the centre line of the shock tube and one that made use of the Schlieren Optical Unit (SOU) seen in Figure 3.9 and 3.10 where the optical axis is twice folded. A schematic drawing of the latter system is presented in figure 3.9. Light is provided with laser. The laser head is mounted outside of the shock tube, perpendicular to it. The beam enters the inner body of the annular section through one of the support struts and expands, thereby illuminating the test section through the glass window. On the receiving side the collimated light is focused with lens L_1 (f=1350 mm) on a schlieren stop. To be able to detect density gradients in all radial directions a circular stop is used. Either a small micro-sphere blocking most of the beam - typically a 0.67

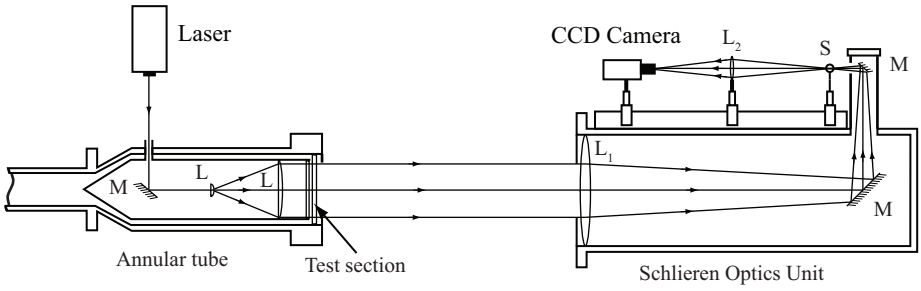

FIGURE 3.9. Schematic drawing of schlieren setup.

mm ball bearing (Figure 3.11) - or a pinhole is used. The former gives dark pictures with light shock waves, while the the latter gives a bright background with darker shock waves.

A second lens L_2 creates an image for the camera. Magnification is decided through choices of lenses L_1 and L_2 and the distances between them and the object plane (the test section). When the SOU is used, the lens L_1 is unchangeable. The straight system which do not use the SOU is in principle no different, excepting that the optical axis is not mirrored.

3.4.1. *Cameras*

Two CCD cameras cameras are used: a PCO SensiCam and a Nikon D80 system camera. The SensiCam (12 bits, 1280x1024 pixels, pixel size: 6.7x6.7 μm) is equipped with a 80 mm Canon lens and can take either singly or multiply exposed images. It is controlled by a computer which receives an external TTL-level trigger signal via a PCI-board. For single exposures, an Nd:YAG laser (New Wave Orion) is used with both cameras. The pulse length of the laser is about $4 - 5$ ns. The timing of the pictures is determined with the laser: the camera was left open for a longer interval (5 μs for the SensiCam and 30 s for the Nikon) and the laser fired at the desired instant for photographing.

The Nikon D80 is a regular digital system camera equipped with a Micro Nikkor 60 mm macro lens. The shutter of the Nikon D80 could not be satisfactory triggered without internal modification of the camera, so the shutter was simply left open for 30 seconds. It was triggered using the pressure comparator described above. At a pressure just below membrane burst pressure, the output triggered a commercial infra-red remote (Nikon ML-L3) which opened the camera shutter. The remote was modified to be triggered by the relay circuit. The delay between the given IR signal and the shutter opening was very long - longer than the propagation time of the shock wave from membrane rupture and focusing, which made it necessary to trigger the camera before the actual membrane opening. Although the optical setup is shielded from stray light, an

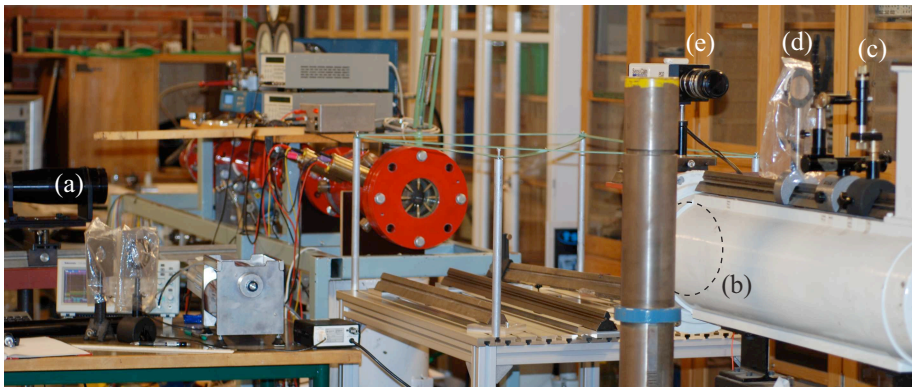

FIGURE 3.10. Setup for schlieren photography: (a) laser light source; (b) 1350 mm lens (inside tube); (c) schlieren stop; (d) focusing lens; (e) camera.

exposure problem occurs with the Nikon camera with the shutter left open for long periods. This causes the camera to not only capture the schlieren image enlightened by the laser beam, but also to be exposed to the implosion light pulse. The implosion pulse may be very bright and over-expose the photograph. The unwanted exposure due to the implosion light flash is damped by placing filters in front of the camera and compensating with increased laser power.

3.4.2. *Lasers*

The Orion laser Q-switch can be triggered internally or externally. In each mode, it first receives a TTL signal to start the flash lamp ("Fire lamp"). In internal QS mode, the laser pulse follows the "Fire lamp" signal after 328 μs. In the external mode, the laser is fired after receiving a second triggering signal ("Fire QS"), typically around 200 μs after the "Fire lamp" signal. The external handling of the Q-switch generates much stronger light than in internal mode. The output laser beam strength is controlled manually. Two energy modes, called High and Low, are available and is supplemented with an energy scale ranging from 0-99. Typical used values was Low 4 with the external Q-switch mode, and Low 15 with internal Q-switch mode. The effective exposure time for schlieren photographs using the Orion laser becomes the laser pulse length, which is 4-5 ns.

Multi-exposed images require a continuous light source. An argon-ion (Spectra-Physics BeamLok 2060) and a HeNe laser were used interchangeably.

3.4.3. *Arrangement procedure*

To arrange the system the following procedure is followed.

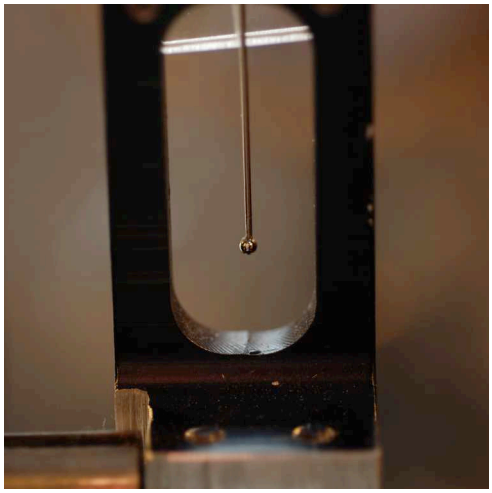

FIGURE 3.11. The etched 0.67 mm micro-sphere used as a schlieren stop.

The first step is to find the optical axis. The axis follows the centre line of the shock tube and is relatively easy to find if the optics are to be aligned in a straight line. However, when the SOU is used the optical axis is twice folded by 90° and SOU must first be aligned. Starting in the camera end might be the simplest course of action. A HeNe laser can be used as an alignment assistant. First, the laser is placed at the position of the camera and the beam is aligned straight with the the optical rail on top of the SOU and directed through the centre of the light hole on the tower. A mirror should be used to control that the beam is aligned along the optical axis of the system. With the laser beam coming out of the SOU along its optical axis, the whole unit can be positioned by moving it until the HeNe beam enters the centre of the shock tube perpendicularly. When properly aligned, the laser beam should go through the whole system and hit the schlieren laser orifice.

Alignment of the schlieren laser is simpler. The surface of the orifice where the beam enters the tube is parallel to the tube centreline, and the laser can therefore be aligned perpendicular to this surface. The alignment of the mirror M inside the tube can be made from outside. A remote-controlled electric motor controls the motion of the mirror around the vertical axis. The motion around the horizontal axis is handled with a manual screw going through the hollow strut on the opposite side of the light-entering strut.

With the SOU and schlieren laser aligned, the optical instruments - lenses, stop and camera - can be placed. Usually the lenses and the camera is placed first, their positions determined by desired magnification. A clear camera image is obtained by putting a semitransparent paper grid in the centre of the test

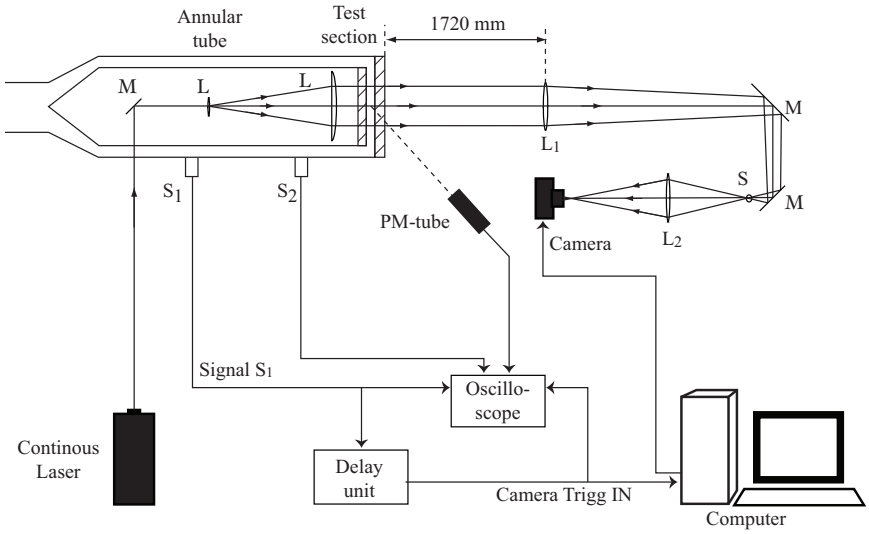

FIGURE 3.12. Diagram of Setup 090420. Description in the text.

section and focusing the camera on the grid. When all optical elements are aligned, the schlieren stop is positioned at the focus point of the laser light.

3.4.4. *Setup example - Multi-exposure schlieren*

Figure 3.12 shows a sketch of a schlieren setup used for multiple-exposure pictures. The lens L_1 has a focal length of 1350 mm and L_2 100 mm. The schlieren stop S was a 0.67 mm ball bearing etched on a thin metal rod. The continuous argon-ion laser and the PCO camera are described above. A delay unit (DGP535 Stanford Systems) and a digital oscilloscope (Tektronix) are used for triggering and monitoring. A signal diagram is shown in figure 3.13, where manually pre-set times are denoted with t_x and measured times with Δt_x. For example, Δt_{S1-S2} is the time the shock wave spends propagating from sensor S_1 to S_2. The triggering is done by the shock sensor S_1. When the shock passes the sensor, a signal is sent to the delay generator. After a pre-determined delay t_{trig} a signal is sent to the computer triggering the camera software (CamWare) to turn on the camera. Exposures t_{exp} and time between exposures t_{xdelay} are set with the camera software. The system is able to handle up to ten individual exposures, each with individual exposure and delay times. Here all ten exposures were set to have equal exposure times and delay. A photo-multiplier tube is used for synchronising the times with the implosion pulse.

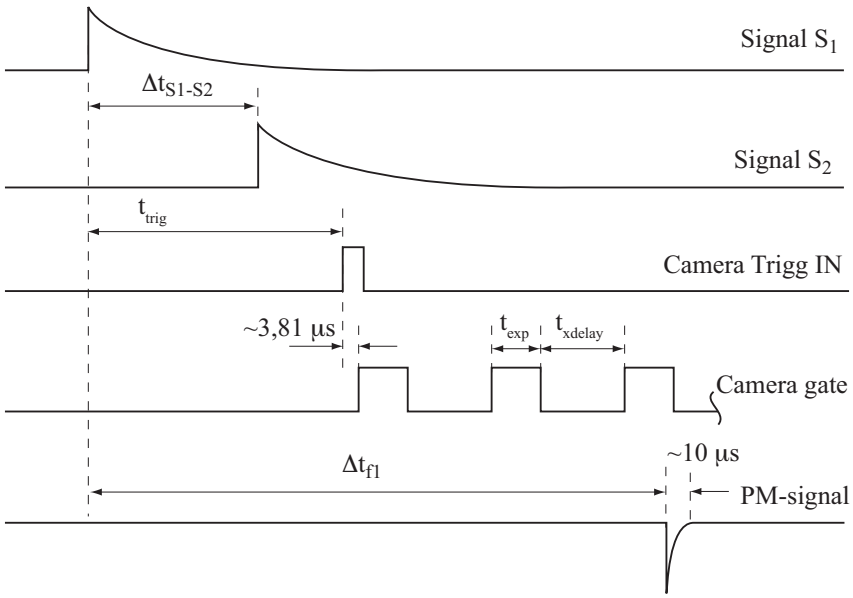

FIGURE 3.13. Timing diagram for Setup 090420. Description in the text. Not to scale.

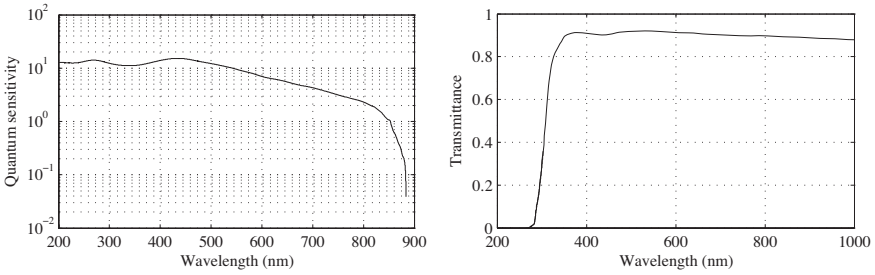

(a) (b)

FIGURE 3.14. (a) Relative CCD wavelength sensitivity and (b) transmittance of the test section glass window.

3.5. Spectrometry

Since the shock focusing creates a bright light pulse, spectrometry is a good non-intrusive way of measuring the gas conditions at the focusing event. The light pulse is about 10 μs long, depending on gas and shock strength, and since it is a most unstationary phenomenon it is desired to break up the pulse in short segments to see the variations.

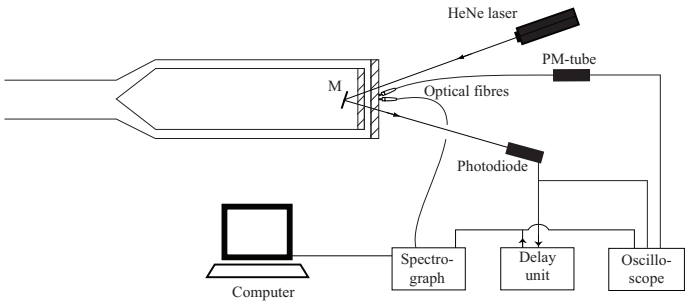

FIGURE 3.15. Spectrometric setup. M, mirror for the laser triggering system.

A schematic drawing of the setup is presented in Fig. 3.15. Light generated at the shock focus is collected by two optical fibres with their openings flush to the glass. One fibre feeds a photomultiplier while the other is connected to a spectrometer (Mechelle 7500, Multichannel Systems, Sweden) with an ICCD camera (Andor Istar). The spectrometer is able to record spectra in the wavelength interval $180 - 880$ nm. The sensitivity of the CCD is dependent on wavelength, which needs to be accounted for when analysing the data. Figure 3.14(a) shows the ICCD sensitivity. The test section glass window also limits the light transmission, to between roughly 350 and 880 nm. The transmittance of the 15 mm thick borosilicate glass is presented in Figure 3.14(b). The spectrometer makes use of an echelle grating, that divides the spectrum into several vertically separated diffraction orders. The complete spectrum is reconstructed by software. The separation causes the sensitivity to drop close to the edges of each order, as can be seen on Fig. 4.12. The spectrometer is wavelength calibrated before the experiments using a Hg lamp. Deviation from theoretical positions of around twelve Hg lines are minimised by a least-square fit method.

The spectrometer unit is triggered by the optical laser triggering method described above. The output from the photodiode amplifier is sent to a time delay unit. A delay is set on the delay unit and the output signal opens the ICCD camera shutter on the spectrometer. Simultaneously the light emission from the focused shock is registered with the photomultiplier. The signals from the photomultiplier, the photodiode amplifier and the ICCD camera trigger pulse are monitored and recorded with a digital oscilloscope. The unknown time delay of the trigger system is measured with a pulse laser and determined with good accuracy. The spectrum exposure times is synchronised with the light flash as measured with the photomultiplier tube with a precision of 10 ns.

3.6. Shock wave shaping

Two different methods have been employed to shape the shock waves into primarily polygonal forms: by cylindrical obstacles creating a reflection and diffraction pattern or by wings dividing the test section into radial channels where plane sides are created.

3.6.0a. *Cylindrical obstacles.* By placing small cylindrical objects in the test section, the diffraction of the converging cylindrical shock wave around the obstacles reshape the overall form. If the size and position of the obstacles are arranged in certain way, symmetrical polygonal forms may be achieved. The diameters of the cylindrical objects ranges from 7.5 to 15 mm. They are positioned between the glass windows using guides. During mounting they are temporarily kept in position with a small amount of glue: equipped with o-rings they are afterwards kept in place mechanically by the pressure from the glass windows.

3.6.0b. *Biconvex wing profiles.* Another method is to place biconvex wings in the test section with their chords aligned radially. The incoming shock wave reflects on the wings and if arranged properly, the shock wave attains polygonal structure with almost plane sides when leaving the channels. Since the wings have sharp leading and trailing edges, less pressure is lost compared to the case when circular objects are used, in which case reflected waves travel upstream. Figure 3.16(a) shows the test section with the wing dividers. The leading edges are aligned flush with the inner surface of the annular channel and the trailing edges end 20 mm from the centre of the test section. Calculations were made to find the appropriate lengths and widths to ensure plane shock wave exiting the channels into the open center of the chamber. One purpose of the wings is to improve the control of shock shaping and to allow the same blockage ratio no matter the number of wings - and consequently the number of sides of the polygonal shock wave - by altering the thickness and length of the wings from case to case. The measurements in the present study however, only feature a configuration with eight such dividers, creating a cylindrical octagonal shock wave.

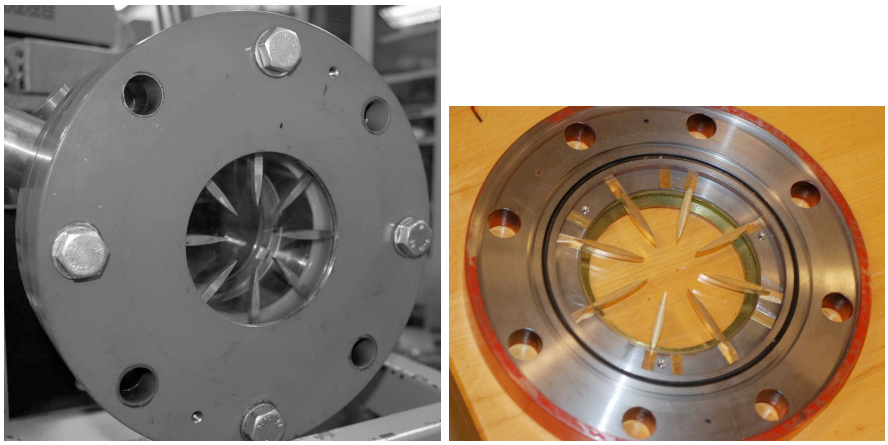

(a) (b)

FIGURE 3.16. Wing matrix mounted in the test section (a) and before assembly (b).

CHAPTER 4

Results and discussion

4.1. Shock propagation

The shock propagation of cylindrical and octagonal shock waves have been studied using non-intrusive schlieren optics. Multi-exposure images allow determination of the velocity and acceleration of the shock waves, while single exposures give sharper images. The reason for this is the light sources: The continuos HeNe laser was much weaker than the pulsed Nd:Yag laser used for single exposures. Also - maybe more importantly - the background lighting was exposed tenfold, which worsened the contrast with the shock schlieren images which were only exposed once.

4.1.1. *Circular shocks*

Fig. 4.1 shows one converging (a) and one diverging (b) circular shock wave in air at different instants. The initial Mach number in the annular section was $M_s = 2.2$ for the converging and $M_s = 2.4$ for the diverging shock wave. Each photo features ten individual exposures of the same shock wave to show the propagation in time. Each of the ten exposures in each picture was 0.3 μs and followed each other by 2.2 μs. The diverging shock wave in 4.1(b) is visibly slower (despite the higher initial Mach number) and distinctly more circular than the focusing shock. In the centre the complex reflections have created a very inhomogenous region as evident from the gradients seen in the image. The reflected shock wave seems to have a constant velocity. In general, a diverging shock wave in an undisturbed medium is decelerating, but since the shock is propagating through a moving gas which is rushing towards the centre with a velocity decreasing with radius, the shock appears to keep constant velocity in the laboratory frame.

As reported in Eliasson (2007), circular shocks in this tube suffer from the four-mode instability caused by the supporting struts of the inner body that was reported by Takayama *et al.* (1987). The collapse of the circular shock shape was further observed. Figure 4.1(a) shows the gradual deformation of the shock front. The sides become increasingly less circular, form straight segments and eventually form corners. Reflections occur in the corners, which can be seen at the last exposure (where r≈0.4 mm). Figure 4.2 shows magnified views of the

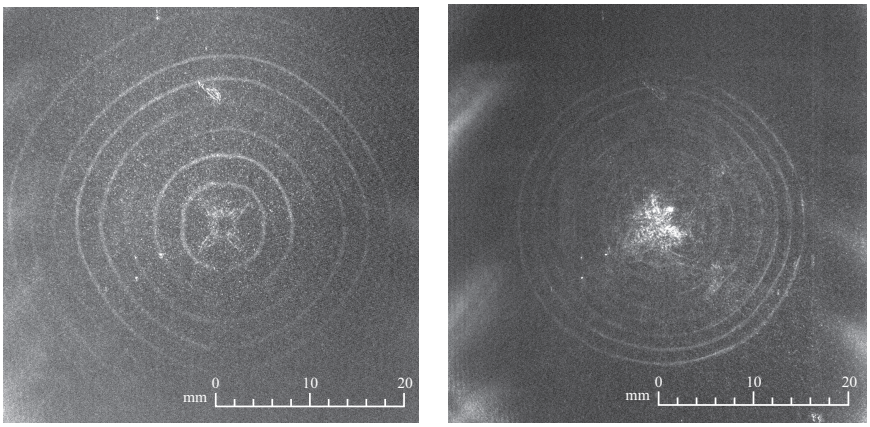

(a) (b)

FIGURE 4.1. Multiply exposed schlieren images of circular cylindrical shock wave: (a) converging shock; (b) diverging shock after focus. The gradual collapse of the circular shape that culminates in the appearance of reflections may be seen in (a). Each exposure is 0.3 μs and the delays between them are 2.2 μs.

circular shock wave collapse. Image Figure 4.2(d) shows the diverging shock wave having re-attained the circular shape.

The relative radius deviation $\Delta r/r$ is a measure of the ability of the shock to preserve its form and a way to quantify stability. Experimental values for circular and octagonal shocks are shown in Figure 4.3. The radius and deviation of the circular shocks have been calculated over the full circle, while the octagonal radius and deviation were calculated from the 8 or 16 midpoints of the plane sides of the shock, thereby being a measure on the ability to keep the polygonal shape. It is worth noting that the deviation of the circular shape in the KTH tube is quantitatively similar to that of the Sendai shock tube as reported by Takayama *et al.* (1987).

4.1.2. *Polygonal shocks*

As reported in Paper 1, the wing matrix dividing the test section in radial channels proved able to create the desired polygonal shock waves. Figure 4.4 shows a series of converging shocks with initial $M_s = 2.4$. Figure 4.4(a) shows the shock wave entering the central, open part of the test section after passing through the channels, where each segment reflects from those emerging from the adjacent channels. Mach stems appear at the intersection. As the incident shocks and Mach stems are almost plane, they propagate at almost constant

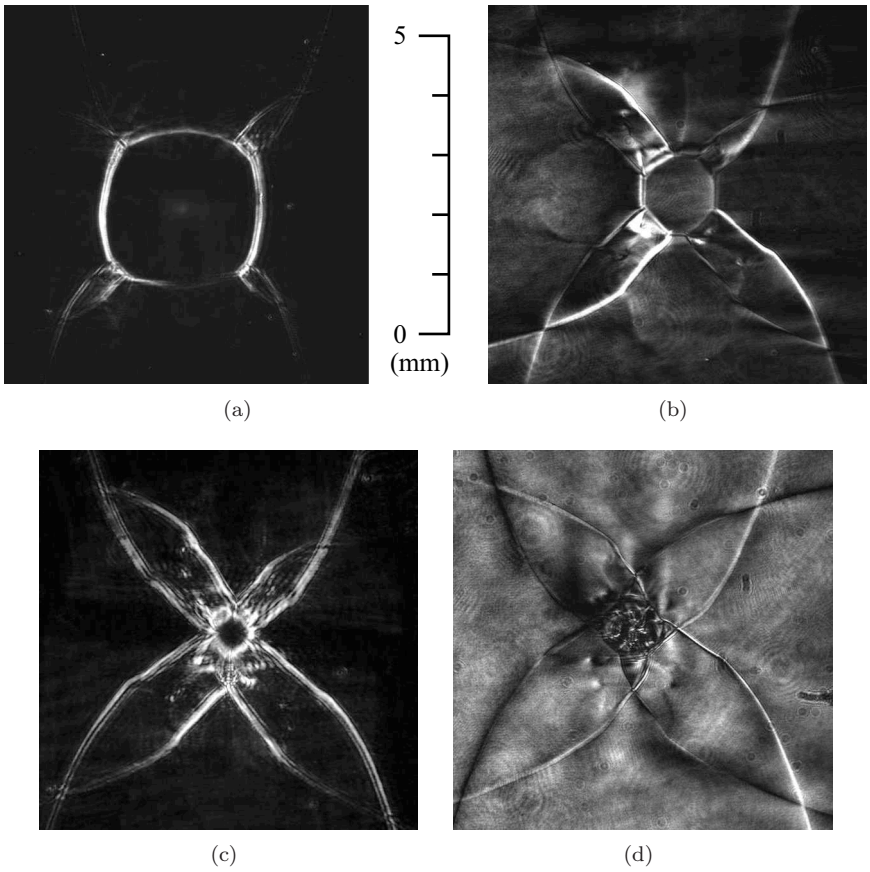

FIGURE 4.2. Schlieren photographs of collapse of cylindrical shock wave. The scale applies for all images. Photos from separate runs.

velocities. Initially short, the stems have higher speeds than the adjacent waves 4.4(a through d). Eventually the Mach stems form a new octagon, rotated by 22.5°, which is accomplished in Fig. 4.4(c). Thereafter the process repeats itself. Much of the acceleration of the polygonal shock wave is therefore due to the Mach reflections. Figures 4.4(e) and (f) show the outgoing, diverging shock which is stable and circular. The diverging shock is influenced by the flow ahead, created by the preceding converging shock.

Schlieren photographs with larger magnification of the polygonal shocks close to focus are shown in Figure 4.5. The shock wave attains a more quadrangular than octagonal shape close to the focus. The front shape of 4.5(b) resembles the collapsed circular front in Figure 4.2(c). Watanabe *et al.* (1995)

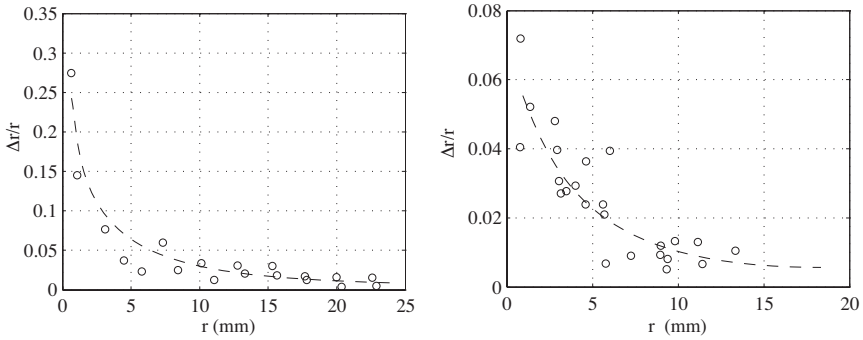

(a) Circular (b) Octagonal

FIGURE 4.3. Deviation from average shock radius for circular and octagonal shock waves.

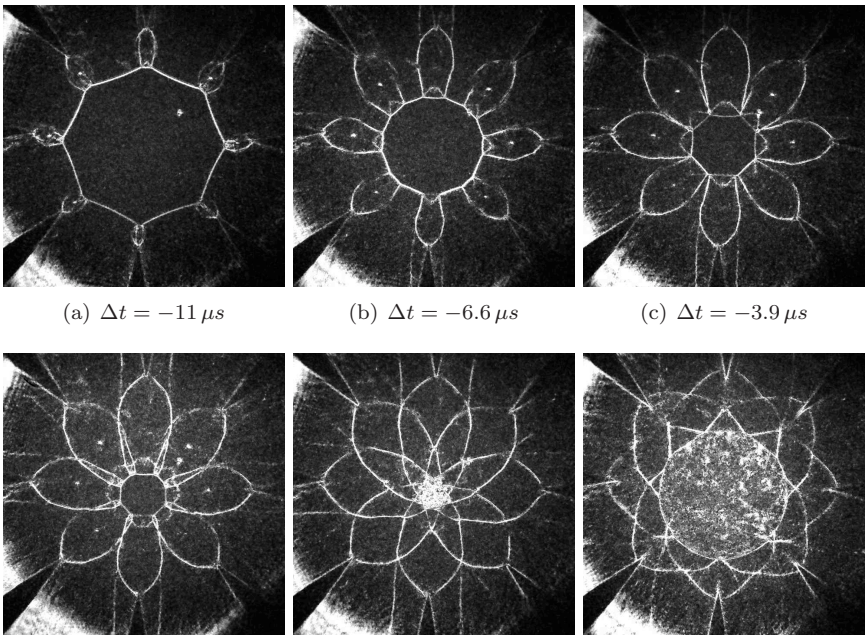

(a) $\Delta t = -11\,\mu s$ (b) $\Delta t = -6.6\,\mu s$ (c) $\Delta t = -3.9\,\mu s$

(d) $\Delta t = -2.56\,\mu s$ (e) $\Delta t = +3.12\,\mu s$ (f) $\Delta t = +17.4\,\mu s$

FIGURE 4.4. Schlieren photographs of converging shock waves in air in the 8-wing configuration. Initial Mach number was $M_s = 2.4$. Times at start of exposure Δt are relative to the implosion event. Each image is from a separate run. The distance between opposite wing tips is 40 mm.

concluded that if there are several perturbation modes in the flow, the lowest would overtake the rest. In other words, the four-mode instability introduced by the struts remains in the flow and becomes more significant closer to the centre. The deformation may also be related to imperfections with the wing or tube alignment. Whatever the cause, it is clear that the information of the eight-configuration is still in the flow behind the shock: the picture of the diverging shock in 4.5(c) shows strong density variations shaped like a gear wheel with eight cogs.

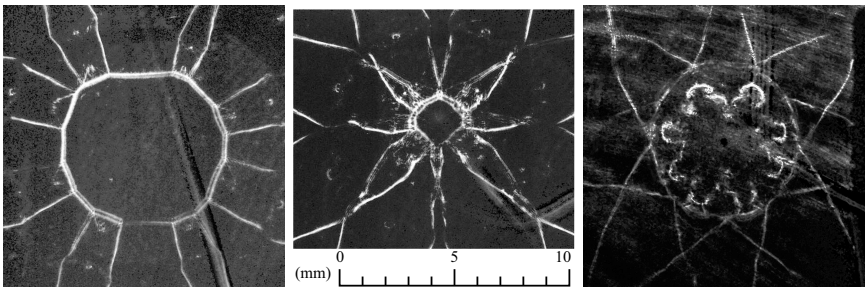

(a) $\Delta t = -1.92\,\mu s$ (b) $\Delta t = -0.50\,\mu s$ (c) $\Delta t = +3.5 - 3.6\,\mu s$

FIGURE 4.5. Schlieren photographs of converging shock waves in air in the 8-wing configuration: (a) and (b) converging shock waves; (c) reflected and diverging shock. Images from different shock tube runs.

Figure 4.6 shows stronger shock waves converging in argon ($M_s = 3.8$, figures (a)-(c)) and air ($M_s = 3.3$, figures (d)-(f)). The shock wave in argon enters the open central test section in very straight segments, but attains an overall square shape in (b). The Mach stems at the axial wings appear to have higher velocities than those emerging from the rotated set of wings. The curvatures of the shocks in 4.6(d-e) compared to those in Figure 4.6(a) and 4.4(a) are noteworthy, showing that the ability of the wings to shape the shock is dependent on gas and shock Mach number. The curved shocks do tend to straighten during the focusing process. The colour has been kept to show the blue-fringed implosion light pulse that was captured by the camera in 4.6(a) through (c).

4.1.2a. *Wing reflections.* The new shocks appearing at the trailing edges of the wings are due to Mach reflections. When the shock waves on each side of the wing arrive at different time instants complex reflections that destroy the symmetry of the overall shape occur. Figure 4.7 shows a series of schlieren images describing such interactions. In (a) the shocks are seen arriving from right to left from the channels. The shocks are a result from the interactions in the channel: an incident shock, a Mach stem and a reflected shock originating in

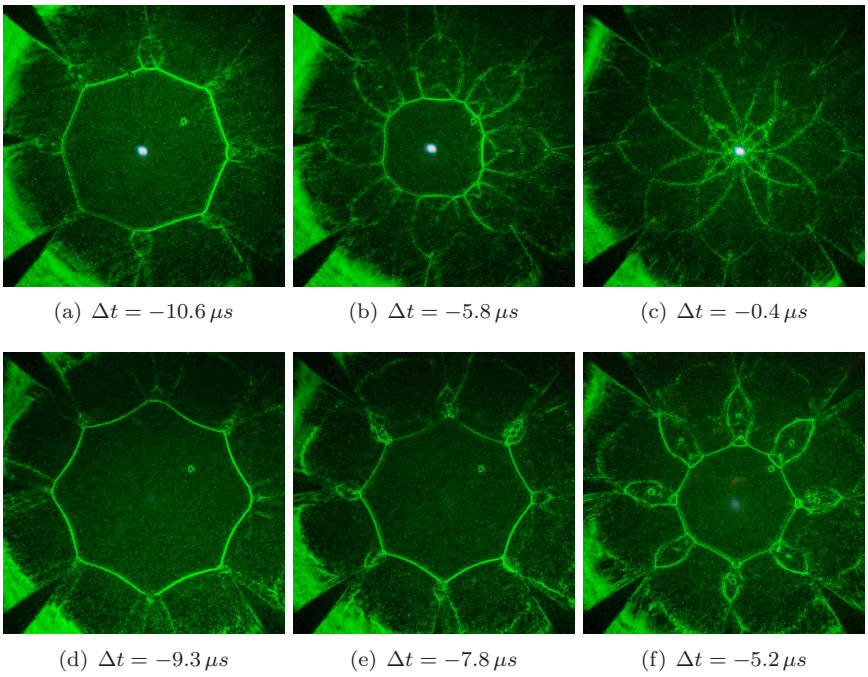

(a) $\Delta t = -10.6\,\mu s$ (b) $\Delta t = -5.8\,\mu s$ (c) $\Delta t = -0.4\,\mu s$

(d) $\Delta t = -9.3\,\mu s$ (e) $\Delta t = -7.8\,\mu s$ (f) $\Delta t = -5.2\,\mu s$

FIGURE 4.6. Schlieren photographs of shock waves with initial $M_s = 3.7$ converging in argon (a-c) and air (d-f). Each image is from a separate run. Times indicate instants of exposure relative to implosion. Images (a-c) also captured the implosion light pulse, which is also seen faintly in (f).

Mach reflections over the leading edge. The reflected shock is travelling towards the wing: it started propagating away from it, reflected on its counterpart from the neighbouring wing and turned back. As the first, lower shock wave arrives at the edge 4.7(b), it curves around it, creating a vortex before striking the upper incoming shock wave. The curved tips of the shocks nevertheless become straight and a pattern resembling transitional Mach reflection occurs 4.7(d). A Mach stem is formed despite the asymmetrical arrival at the tip, but the pattern is shifted upwards and this has an impact on the focusing process.

4.1.3. *Inner body alignment*

The eccentricity of the inner body inside the shock tube has major impact on the symmetry of the shock waves. Referring to Figure 3.1, the inner body is supported by two sets of struts. The downstream set is located close to the test section and may be aligned with the help of a mechanical guide. The upstream set is situated too far upstream for this method to be useful. It was found that

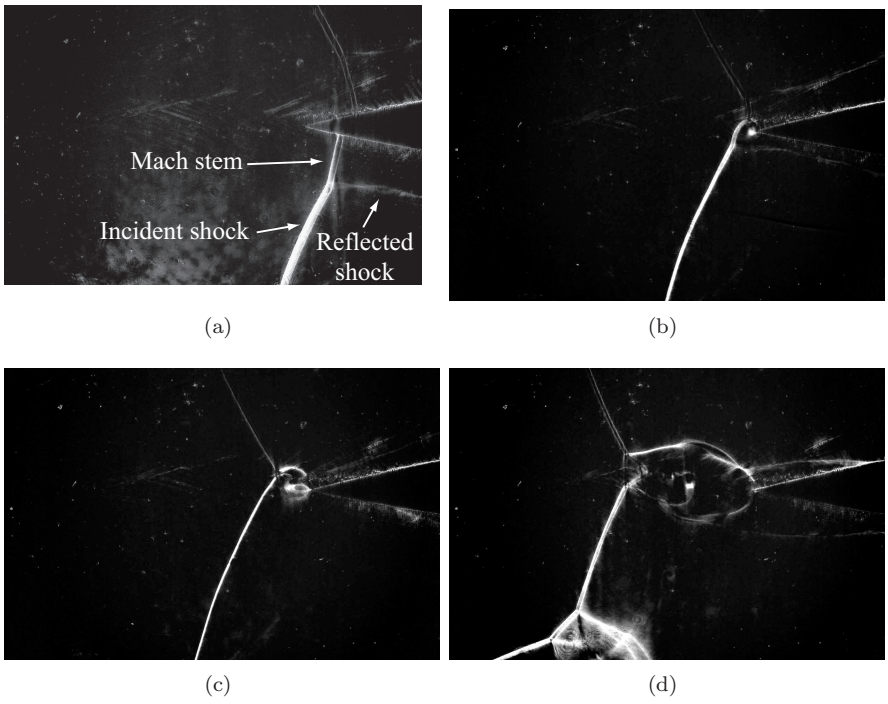

FIGURE 4.7. Reflection of two shock waves arriving at wing edge at slightly different times. Each image is from a separate run.

the wings provided a good tool for tuning the position of the body. The wing matrix divided the test section in eight radial channels and the velocity of each segment of the otherwise connected circular shock wave could be seen in detail. Figure 4.8 shows schlieren photographs of shock waves exiting the channels. The shocks have clearly different velocities as they arrive at different instants. This suggests that the inner body is eccentric with the annular channel being slightly narrower at the part of the channel corresponding to the position of the faster shocks and vice versa. To ensure that asymmetric construction of the matrix did not give rise to the irregularities, the matrix was gradually rotated between several runs. The shock pattern was unchanged with rotation and it was concluded that the matrix construction was good. The struts were adjusted accordingly to the schlieren photographs. By trial and error the arrival of the shock fronts at the end of the matrix could be improved. Figure 4.8 (a) shows the shock pattern before alignment: the whole lower half of the shock seems faster than the upper. This corresponds well with the shock focus being found slightly below the geometrical centre, as reported below. Figure 4.7

shows reflections around the right-most encircled wing-tip in Figure 4.8(a). Figure 4.8(b) shows the pattern after alignment: the general shape is much improved, but one segment could not be made to arrive simultaneously with the others (arrow). It is speculated that this is due to other affects, such as off-axis alignment of the wing-shaped profiles the struts are made of. The photomultiplier signal measuring the implosion pulse showed an increase in strength after the alignment. This work was made in December 2009 and it is suggested that new schlieren images are taken at a later date to determine if the inner body settles or moves over time.

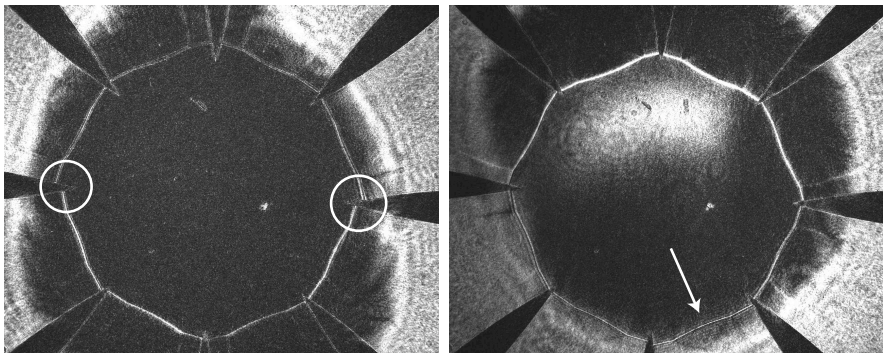

(a) (b)

FIGURE 4.8. Schlieren images of shocks arriving at the open center of the test section to illustrate the effect of non-aligned inner body: (a) before and (b) after alignment.

4.2. Comparison of theory and experiments

Comparisons with Guderley's self-similarity solution have been made of the form (rewritten from chapter 2):

$$\frac{r}{R_c} = \left(1 - \frac{t}{t_c}\right)^a \tag{4.1}$$

where t_c is the time it takes for the shock to travel from R_c to implosion centre. Fits were made from experimental data from multiple-exposure schlieren photographs. The power law fits are extremely sensitive to the values of t_c. Special care was therefore taken to determine the moment of implosion. The values for R_c had less influence on the calculated values of a. The exponent was calculated for eight shots in air at different Mach numbers (2.2-3.4). The acquired mean value was $a = 0.836$, and varied between 0.824 and 0.846. No dependence on Mach number was seen: the variance was largely due to the determination of t_c. This is in good agreement with analytical data. (see

Table 2.5.1). Figure 4.9 shows a propagation diagram of circular shocks (a) and a log-plot showing the average self-similarity exponent. Lack of sufficient data prohibited good determination of an exponent for shock waves in argon: only one image was available, with few data points, from which an exponent $a = 0.82 \pm 0.05$ was found.

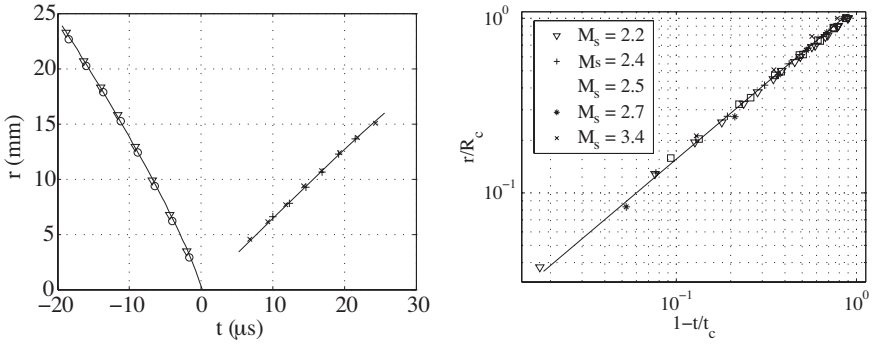

(a) (b)

FIGURE 4.9. Comparison of measured propagation of circular shock wave in air with the Guderley power-law solution: (a) experimental data from two converging $(O, \bigtriangledown)$ shocks compared with power-law fit with $a = 0.836$ (full line) and two diverging $(+, \times)$ shocks; (b) log-log plot of converging shock waves in air at different initial M_s.

The polygonal shock wave follows approximately a power-law solution like Eq. 4.1, but with slower convergence than circular shocks. Results are presented in paper 1.

4.2.1. *Light emission*

Measurements of the light emission from shock waves converging in argon was made. The diaphragms had thickness of 0.5 mm and helium was used as driver gas, yielding an initial Mach number $M_s = 3.8$.

The light flash has a total duration of roughly 10 μs for the 8-wing configuration. Photomultiplier records from more than a hundred runs using various combinations of gases show a fairly reproducible strength of light intensity for each set of gas combinations. The set presented in Fig. 4.10 shows the signals from twenty runs. The negative peak signal strength varies little, with a mean value of -0.49 V and standard deviation 0.02 V. The spread increases after the collapse. The actual fall time is short, about 12 ns, but is preceded by a small decrease in output voltage prior to the peak. This indicates that the gas behind the shock starts to emit light at least 100 ns before the actual focusing

instant. The variation of the signal strength may be compared to the circular case, where a series of twenty runs showed a mean of -0.52 V and a standard deviation 0.17 V. The absolute intensity can unfortunately not be compared directly, as the photomultiplier tube had slightly different positions.

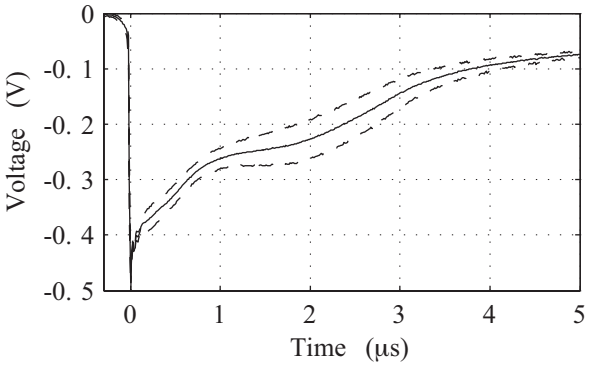

FIGURE 4.10. Photomultiplier records of light emissions from converging polygonal shock waves in argon: mean value and standard deviation (dashed lines) from twenty runs.

Various photographs of the emitting gas core at the instant of shock implosion in the 8-wing configuration are shown in Fig. 4.11. The camera was a Nikon D80 equipped with a Macro Nikkor 60 mm lens. The images were taken by leaving the shutter open for a long time (bulb mode or 30 s). In image 4.11(a) the lights in the laboratory were simply turned off and a large aperture was used in order to demonstrate how the light looks to the naked eye. Photographs 4.11(b)-(d) were taken from a light-sealed compartment around the end section of the tube and the only light source was the radiating gas. The aperture was set at minimum to show the bright core, but parts were till over-exposed. The images 4.11(b) and (c) are taken from an oblique angle to show the extent of the radiating core: the emitting volume at the focus is seen to have the form of a thin cylinder, stretching the full 5 mm span between the framing windows of the test section. This indicates that the polygonal shock convergence in the test chamber preserves the two-dimensional structure of the shock to the end of the focusing process.

The position of the radiating core - and the variation thereof - was determined in a simple fashion. The camera was placed in front of the test section, zooming in on a 33x23 mm area around the centre. A number of shots were taken and the position of the core determined by overlay of a photograph of a graded paper. One example photo is shown Figure 4.11 (d). The focal point of the converging shocks was found shifted from the geometrical centre by 2 mm

downwards. This determination of focus position was made before the centering of the inner cone, which prior to the tuning did have an eccentricity in the vertical direction. New measurements should be made to see the effect of the alignment. No quantitative measurements on the spacial intensity distribution were made.

The colour temperature is believed to be well reproduced in the photographs. The colour of the emitting core shifts between the white and blue, presumably depending on focal symmetry. A blue shift is generally connected with higher blackbody temperatures.

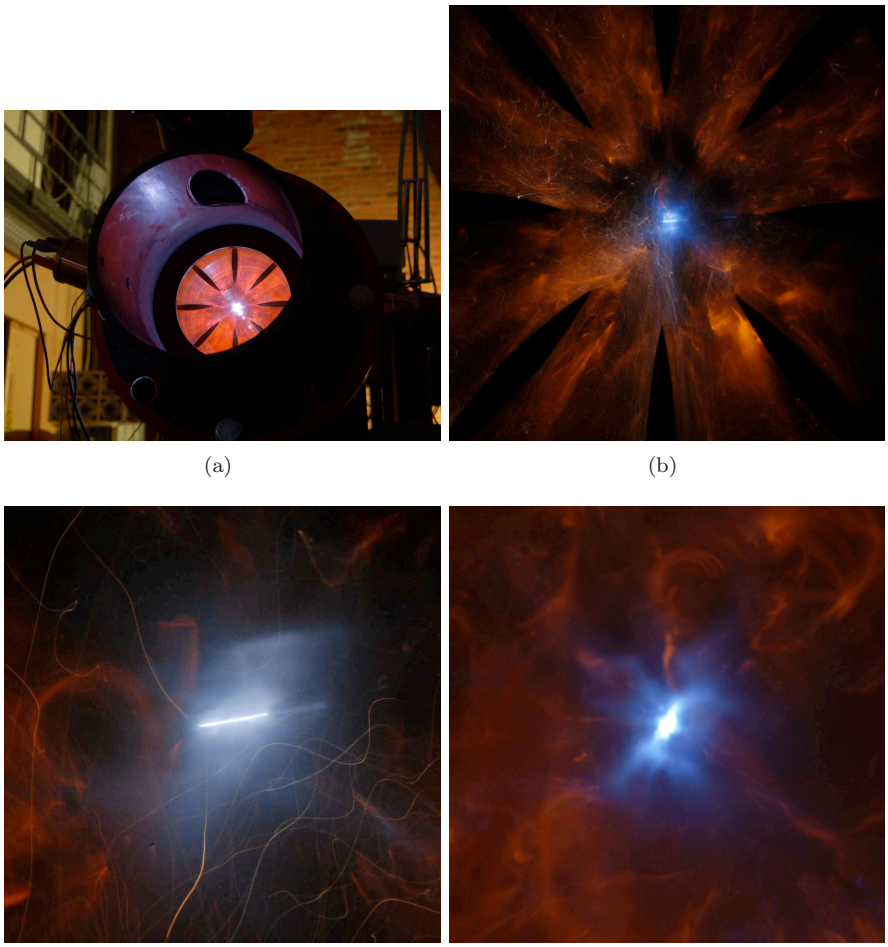

(a) (b)

(c) (d)

FIGURE 4.11. Photographs of implosion light pulse.

4.2.1a. *Spectrometry.* The light emission from shocks converging in argon with the 8-wing configuration have been measured spectrometrically and the results are presented in Paper 1. Here is a short summary and some complementary results. The emission has been measured both in its entirety and divided into a sequence of 60 ns long exposures. Fig. 4.12(a) shows a time-integrated spectrum, taken with the shutter open during the whole emission interval. The data shows continuum radiation, on which a series of emission lines is superimposed. The emission lines originate from electron transitions between excited states in neutral argon atoms. The effects of the echelle prism in the spectrometer can be seen in the bumpy appearance of the continuum. Each parabola corresponds to one order, and shows the sensitivity drops at the edges of each order. These drops are due to the equipment construction, and are not related to the light emission. Fig. 4.12(b) shows an overview of the 60 ns spectra. The continuum appears at the implosion, while the line Ar I emission becomes distinct about 1 μs after the peak.

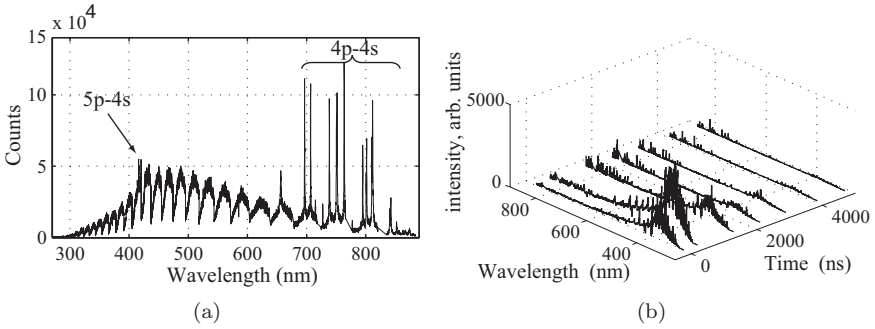

FIGURE 4.12. Uncorrected time-integrated spectrum of implosion light pulse in argon (a) and time-resolved spectra over the complete pulse (b).

The continuum radiation measured in the 60 ns spectra was compared to the blackbody function,

$$I(\lambda, T) = \frac{2hc^2}{\lambda^5} \frac{1}{\exp(hc/\lambda kT) - 1} \tag{4.2}$$

where h is the Planck constant and c the speed of light. A least squares method was used and corrections made for the quantum efficiency of the camera and the transmission losses in the glass window. Results showed a highest blackbody temperature in the beginning of the light pulse, 5800±200 K. Figure 4.13 displays the evolution of the gas temperature from these fits.

A number of emission lines originating from electron transitions in neutral argon were detected. The identified transitions are between either the $3p^5 4p$ or

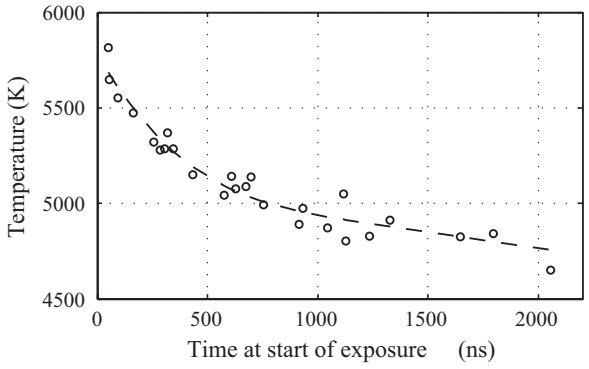

FIGURE 4.13. Blackbody temperatures acquired from 60 ns spectra.

$3p^5 5p$ manifolds, and the first level of excited states in argon, $3p^5 4s$. Transitions from the $3p^5 5p$ level were only observed in the time-integrated spectrum; the significantly lower intensities drowned in the noise in the 60 ns window spectra. These states corresponds to energy levels around 14.7 eV, which may be compared with the ionisation level of 15.8 eV. Possible transitions from these states to the ground state have wavelengths below the detection range. Table 4.2.1a lists the most prominent lines, which are shown in Figure 4.14.

A common method to determine the temperature of the excited gas is the Boltzmann plot. Based on the assumptions of local thermodynamic equilibrium and that the intensity of an atomic line emission from a certain state to another is directly proportional to the number density of the atoms in the states, a relatively simple linear relation between the temperature and intensity is acquired :

$$ln\left(\frac{\lambda_{ij} I_{ij}}{g_i A_{ij}}\right) = -\frac{E_i}{kT} + const \tag{4.3}$$

Where I_{ij} is the intensity of the emission line λ_{ij}, g_i is the degeneracy of the upper level E_i. Plots of E_i versus the left hand side of Equation 4.3 for lines terminating in the same lower state j should yield a line from which the temperature may be determined. Plots based on the 60 ns spectra were made, but the result was not linear. Generally this is an indication that the radiating gas not being in LTE. In this case the energy levels were all very close, meaning that accurate fits are difficult to make. Further, the light was collected from a large radiating volume with likely in-homogenous gas conditions. Therefore we draw no conclusions yet. Future measurements should be spatially resolved to deal with this problem.

λ_{ij} (nm)	Transition	E_i (cm^{-1})	g_i	$A_{ij}(s^{-1})$
415.9	$5p - 4s$	117184	5	1.40×10^6
420.1	$5p - 4s$	116943	7	9.67×10^5
430.0	$5p - 4s$	116999	5	3.77×10^5
696.5	$4p - 4s$	107496	3	6.39×10^6
706.7	$4p - 4s$	107290	5	3.80×10^6
714.7	$4p - 4s$	107132	3	6.25×10^5
727.3	$4p - 4s$	107496	3	1.83×10^6
738.4	$4p - 4s$	107290	5	8.47×10^6
750.4	$4p - 4s$	108723	1	4.45×10^7
751.5	$4p - 4s$	107054	1	4.02×10^7
763.5	$4p - 4s$	106238	5	2.45×10^7
794.8	$4p - 4s$	107132	3	1.86×10^7
800.6	$4p - 4s$	106238	5	4.90×10^6
801.5	$4p - 4s$	105617	5	9.28×10^6
810.4	$4p - 4s$	106087	3	2.5×10^7
811.5	$4p - 4s$	105463	7	3.31×10^7
840.8	$4p - 4s$	107290	5	2.23×10^7
842.5	$4p - 4s$	105617	5	2.15×10^7

TABLE 3. Detected lines from electron transitions in neutral argon. Data from NIST (2008).

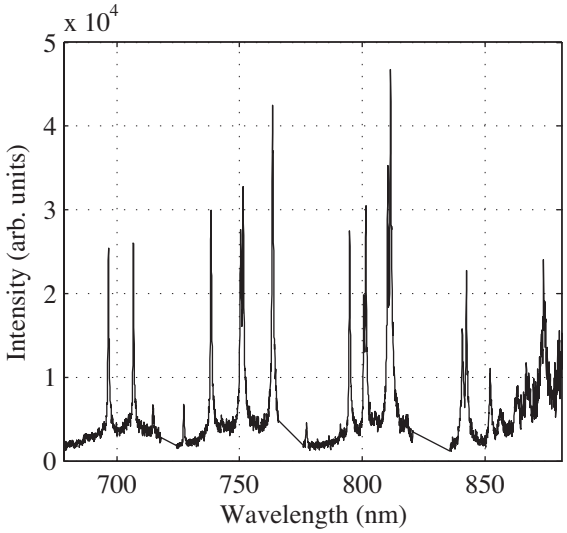

FIGURE 4.14. Corrected emission lines from transitions between the low-lying electronic shells in atomic argon.

CHAPTER 5

Numerics

This chapter is an introduction to the analytical or numerical methods used to solve the problem with converging shock waves. The problem formulation consists of a cylindrical or spherical shock wave of an initial Mach number M_0 and radius r_0 converging in a monatomic gas. The shock position has a radius r with an area $A(r)$. The Mach number M and the thermodynamic equilibrium conditions behind the shock are to be determined for all shock positions.

5.1. Shock dynamics

Whitham's solution to the converging shock problem using geometrical shock dynamics is based upon the assumption that the shock wave propagates along rays being C_+ characteristics.This approximation has been shown to provide accurate results Whitham (1973),Apazidis *et al.* (2002),Hornung *et al.* (2008) especially for continuously accelerating shocks. Consider a shock propagating down a tube with a cross-section $A(x)$. The problem can be approximated as a quasi one-dimensional if the area change is not too rapid. The characteristic equation along the C_+ characteristic states that (Whitham (1973)):

$$\frac{dp}{dx} + \rho a \frac{du}{dx} + \frac{\rho a^2 u}{u+a} \frac{1}{A} \frac{dA}{dx} = 0 \tag{5.1}$$

Where p is the pressure, u the velocity and a the speed of sound behind the shock wave. Using the Rankine-Hugoniot relations without consideration for ionisation this can be reformulated into an area-Mach-number relation, from where the propagation can be determined.

This non-reacting perfect gas approach has shown good agreement with experimental data concerning shock front propagation. However, as the shock falls in on the focus, it predicts the temperature and pressure to increase exponentially towards infinity. In order to allow for reactions, a solution is instead sought by directly integrating Eq. 5.1 without making any simplifications. The spatial coordinate x is changed to r for clarification since only radially symmetric geometries are considered here. For a cylinder or sphere the surface area is $A(r) = 2\pi(\nu - 1)r^{\nu-1}$, where $\nu = 2$ or $\nu = 3$ for the respective case. Inserting the derivative of A and differentiating, Eq. 5.1 is rewritten as:

$$dp + \rho a du = -\frac{\rho a^2 u}{u+a}\frac{(\nu-1)}{r}dr \tag{5.2}$$

Integrating between two conditions 1 and 2, corresponding to two Mach numbers $M = M_1$ and $M = M_2$ we get:

$$\int_1^2 \frac{u+a}{\rho a^2 u}dp + \int_1^2 \frac{u+a}{au}du = -(\nu-1)\ln\frac{r_2}{r_1} \tag{5.3}$$

The radius of the shock wave at two consecutive time instants can be expressed as:

$$r_2 = Q_{1-2}r_1 \tag{5.4}$$

$$Q_{1-2} = \exp\left(-\frac{1}{(\nu-1)}\left[\int_1^2 \frac{u+a}{\rho a^2 u}dp + \int_1^2 \frac{u+a}{au}du\right]\right) \tag{5.5}$$

Starting from an initial mach number M_1 and radius r_1, the shock front propagation can now be calculated. The change in radius as the shock wave accelerates to a new Mach number $M_2 = M_1 + dM$ is acquired by calculating the post-shock conditions for M_1 and M_2, accounting for ionisation as described in Chapter 2, inserting into Eq. 5.4 and evaluating the integral numerically. The speed of sound, a, is now taken as the equilibrium speed of sound in a partially or completely ionised gas.

5.2. Euler solver

Numerical calculations were made with a two-dimensional Euler solver on an unstructured triangular grid with adaptive mesh refinement. The scheme is the artificially upstream flux vector splitting (AUFS) scheme introduced by Sun & Takayama (2003). The fundamental idea is to overcome the disadvantages of up-winding schemes by introducing artificial wave speeds into the flow which simplifies the discretisation. The implemented scheme used for the calculations is presented here; the detailed derivation can be found in the cited article. In Cartesian coordinates, the Euler equations on conservative form is formulated:

$$\mathbf{U}_t + \mathbf{F}_x + \mathbf{G}_y = 0 \tag{5.6}$$

where $\mathbf{U}$ and $\mathbf{F}$ and $\mathbf{G}$ are the conserved primitive variables and fluxes:

$$U = \begin{pmatrix} \rho \\ \rho u \\ \rho v \\ \rho E \end{pmatrix}, \qquad F = \begin{pmatrix} \rho u \\ \rho u^2 + p \\ \rho v u \\ \rho E u + p u \end{pmatrix}, \qquad G = \begin{pmatrix} \rho v \\ \rho u v \\ \rho v^2 + p \\ \rho E v + p v \end{pmatrix} \tag{5.7}$$

where the total energy $E = e + u^2/2$ is the sum of the internal energy e and the kinetic energy per unit mass. On a Cartesian grid, a conservative 1st order scheme to solve Equation 5.6 is:

$$\mathbf{U}_{i,j}^{n+1} = \mathbf{U}_{i,j}^{n} - \frac{\Delta t}{\Delta x_{i,j}}(\mathbf{F}_{i+1/2,j} - \mathbf{F}_{i-1/2,j}) - \frac{\Delta t}{\Delta y_{i,j}}(\mathbf{G}_{i,j+1/2} - \mathbf{G}_{i,j-1/2}) \quad (5.8)$$

where i and j refer to the grid centres and $i + 1/2$, etc, to the interfaces between them. In our calculations, unstructured triangular meshes have been used. Referring to the grid cell illustrated in Figure 5.1, Equation 5.8 may be formulated and calculated over the normal interfaces between the cells. Variables denoted L refers to the states inside the cell and R to those in the neighbouring cells.

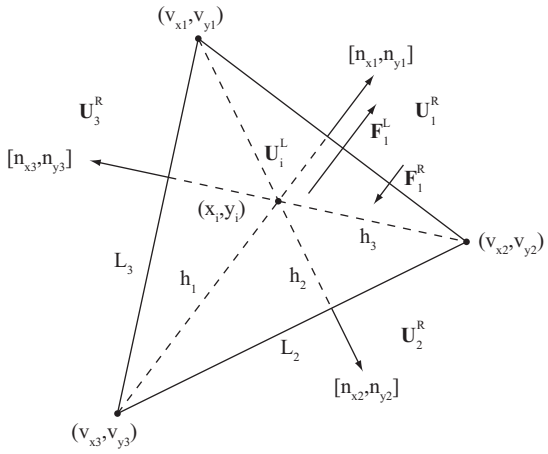

FIGURE 5.1. Typical grid cell i. $\mathbf{U}_i^L$ is the state in the cell while $\mathbf{U}_j^R, j = 1, 2, 3$, are the states in neighbouring cells.

$$\mathbf{U}_t + \mathbf{F}_n = 0 \leftrightarrow \mathbf{U}_t + \mathbf{A}\mathbf{U}_n = 0 \quad (5.9)$$

where $\mathbf{A}$ is the Jacobian matrix $A_{ij} = \partial F_i/\partial U_j$ and n refers to the normal direction. The matrix $\mathbf{A}$ has four real eigenvalues corresponding to the four wave speeds of the system, $(u_n - a, u_n, u_n, u_n + a)$, where $u_n = un_x + vn_y$ is the normal velocity across the interface. Provided that $u_n < c$ somewhere, the system therefore contains waves going both upstream and downstream which makes up-winding difficult. However, observed from some frame of reference all waves propagate in the same directions. By introducing the artificial wave speeds s_1 and s_2 corresponding to such a moving frame of reference the flux

can be rewritten to simplify the discretisation. The flux becomes, after some manipulation:

$$\mathbf{F} = (1-S)\mathbf{F}_1 + S\mathbf{F}_2 = (1-S)\left[\frac{1}{2}(\mathbf{P}^L + \mathbf{P}^R) + \delta\mathbf{U}\right] + S\left[\mathbf{U}^d(u_n^d - s_2) + \mathbf{P}^d\right] \tag{5.10}$$

where $S = s_1/(s_1 - s_2)$, $\delta\mathbf{U}$ artificial viscosity, $\mathbf{P} = (0, pn_x, pn_y, pu_n)$ and d is either L (if $s_1 > 0$) or R (if $s_1 \leq 0$) , depending on whether the corresponding wave go into or out of the cell. The pressure is acquired from the internal energy: $e = p/(\gamma - 1) = E - u^2/2$ (the temperature is attained from the perfect gas law). The artificial viscosity term is:

$$\delta\mathbf{U} = \frac{1}{2\bar{a}}\begin{pmatrix} p^L - p^R \\ (pu)^L - (pu)^R \\ (pv)^L - (pv)^R \\ \frac{\bar{a}^2}{\gamma-1}(p^L - p^R) + \frac{1}{2}((pU^2)^L - (pU^2)^R) \end{pmatrix} \tag{5.11}$$

where $U^2 = u^2 + v^2$ and $\bar{a} = (a^L + a^R)/2$ is the average speed of sound of domains L and R. The artificial wave speeds were chosen as

$$s_1 = \frac{u_n^R + u_n^L}{2} \tag{5.12}$$

$$s_2 = \begin{cases} min(0, u_n^L - a^L, u_n^* - c^*) & s_1 > 0 \\ max(0, u_n^* + c^*, u^R + v^R) & s_1 \leq 0 \end{cases} \tag{5.13}$$

$$u^* = \frac{1}{2}(u_n^L + u_n^R) + \frac{a^L - a^R}{\gamma - 1} \tag{5.14}$$

$$c^* = \frac{1}{2}(a^L + a^R) + \frac{1}{4}(\gamma - 1)(u_n^L - u_n^R) \tag{5.15}$$

Again, for details of the derivation the reader is to directed to Sun & Takayama (2003). The solution update for the grid i between timesteps n and $n + 1$ is then calculated by a first-order method, where the timestep Δt is determined from the CFL condition:

$$\mathbf{U}_i^{n+1} = \mathbf{U}_i^n - \sum_{k=1}^{3} \frac{\Delta t}{h_k}\mathbf{F}_k \tag{5.16}$$

5.2.0b. *Ionising shocks.* Ionisation effects may be introduced by modifying the energy and state equations accordingly. In the calculations only one level of ionisation was included since it was apparent that the number of ions with charge state $i = 2$ or more were negligible for cylindrical shock waves with the initial parameters of the experiments. However, we present here the general

equations for any number of stages of ionisation. Local thermodynamic equilibrium is assumed to be established everywhere in the flow and the additional variables are the ionisation fractions α_i.

The primitive variables are the same, as is the up-winding scheme with modifications to the speed of sound which is presented further below. In the non-ionising case, the pressure is acquired directly from the energy and the temperature from the equation of state. A similar approach is taken in this case. The equation of state and internal energy, neglecting Coulomb forces and excitation energy, are now:

$$p = (1 + \alpha_e)\rho RT \tag{5.17}$$

and

$$e = \frac{3}{2}(1 + \alpha_e)RT + R\sum_{i=1}^{\ell}\left(\alpha_i \sum_{j=1}^{i}\frac{I_j}{k}\right) \tag{5.18}$$

where α_e is the average ionisation fraction and I_j are the ionisation potentials as defined in chapter 2. With the additional variables α_i the system is closed with the Saha equations which can be expressed as functions of T and ρ and solved in the same manner as presented by Trayner & Glowacki (1995):

$$\frac{\alpha_{i+1}}{\alpha_i} = \frac{1}{\alpha_e}\left(\frac{2\pi m_e}{h^2}\right)^{3/2}\frac{m_H(kT)^{3/2}}{\rho}\frac{2Q_{i+1}^{el}}{Q_i^{el}}\exp\left(-\frac{I_{i+1}}{kT}\right) \tag{5.19}$$

where m_H is the mass of the neutral atom. Solving the equation in terms of a given primitive variable ρ instead of p is preferred, since the latter is a derived variable.The temperature and ionisation fractions for each grid are carefully balanced and calculated from the given primitive variables during each time-step. An iterative method is used to find the ionisation and temperature that fulfils the energy requirement 5.18 as well as the set of Saha equations 5.19. This implies finding the root of the transcendental equation $T - f(\alpha_e(T,\rho)) = 0$, where the numerically evaluated function f is determined from the known energy 5.18. Explicitly written out this becomes:

$$T - \left[e - R\sum_{i=1}^{\ell}\left(\alpha_i(T,\rho)\sum_{j=1}^{i}\frac{I_j}{k}\right)\right]\left[\frac{3}{2}(1 + \alpha_e(T,\rho))R\right]^{-1} = 0 \tag{5.20}$$

Equation 5.20 may be solved by a bi-section method with initial lower bound $T = T_0$ and upper bound set to the ideal non-ionising temperature. Once the temperature and ionisation fractions are found, the pressure is extracted from the equation of state 5.17.

The artificial wave speeds s_1 and s_2 are chosen in the same manner as previously, but the speed of sound now becomes the equilibrium speed of sound, $a_e = (\partial p/\partial \rho)_s$, which can be calculated from derivatives of α (see Appendix A).

5.2.0c. *Single ionisation.* When only one stage of ionisation is likely to be present, Eq:s 5.19-5.20 can be simplified to significantly reduce calculation time. Such a scheme has been presented in Aslan & Mond (2005). Only one Saha equation remains, for $i = 1$ where $\alpha_0 = 1 - \alpha_1$, which does not need iteration. In this temperature range, the partition function ratio can be adequately approximated by a constant ($2Q_1/Q_0 \approx g_0 \approx 11$) and Eq 5.19 reduces to:

$$\frac{\alpha_1^2}{1-\alpha_1} = g_0 \left(\frac{2\pi m_e}{h^2}\right)^{\frac{3}{2}} \frac{m_H (kT)^{3/2}}{\rho} \exp\left(-\frac{I_1}{kT}\right) = g_0 C \frac{T^{3/2}}{\rho} \exp\left(-\frac{I_1}{kT}\right) \tag{5.21}$$

where the constant $C \approx 1.603 \times 10^{-4}$ kg·m^{-3}·K$^{-3/2}$ for argon.

The approximation of the partition function ratio as a constant carry a certain error, which is exemplified in Fig. 5.2 and 5.3. The post-shock conditions resulting from the approximation are compared to those where the partition functions included a summation over the first few terms. As evident, the error is reasonably small until $M \approx 30$, around where the second stage ionisation becomes significant (compare with Fig. 2.2). At high T full ionisation occurs in both cases and the thermodynamic variables approach the same values.The calculations are made with initial pressure 0.1 atm and $T = 300$ K.

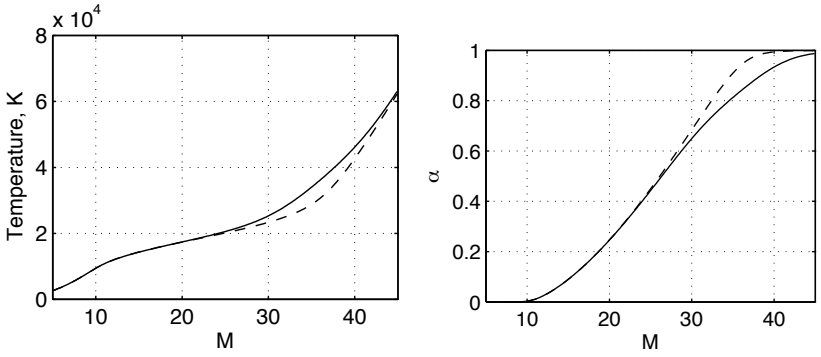

(a) (b)

FIGURE 5.2. Error caused on shock relations by the assumption $Q_1/Q_0 = 11$ (dashed line) compared to $Q_1/Q_0 = f(T)$.

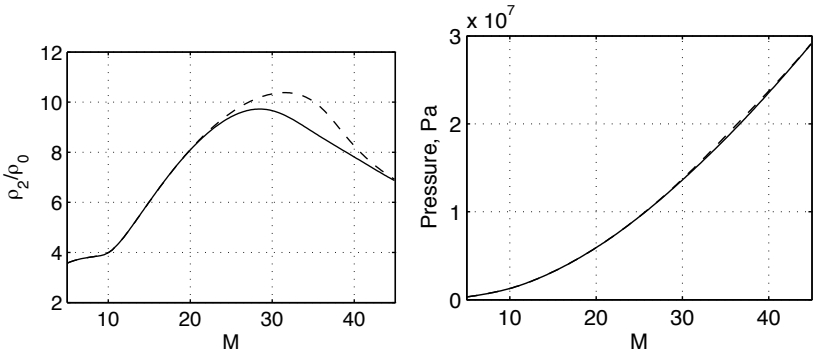

(a) (b)

FIGURE 5.3. Error caused on shock relations by the assumption $Q_1/Q_0 = 11$ (dashed line) compared to $Q_1/Q_0 = f(T)$.

5.2.1. *Test cases*

Calculations were made to compare with the experimental data. The AUFS scheme without ionisation was implemented on unstructured triangular meshes. Two geometries were used, one completely circular and one with eight wing profiles. The meshes were circular with a radius of 80 mm, corresponding to the test section and the annular tube which measure 70+10 mm. The number of cells of the circular mesh was approximately 7×10^5, with the density of grid cells increasing sharply closer to the focal point. The mesh was refined along boundaries and sharp edges.

Two basic cases for each geometry computed corresponding to the experimental cases: one shock wave in argon with initial Mach number $M_s = 3.8$ and one in air with $M_s = 2.4$. The initial conditions was set as two regions: and undisturbed field for $r < 70$ mm with initial pressure 10 kPa and temperature 300 K. Outside the undisturbed region the initial conditions was set to a shocked state corresponding to the respective Mach numbers.

A detail from the eight-wing mesh is presented in Fig. 5.4, which shows a comparison of experimental (white on black) and numerical (black on white) schlieren images. A blow up of a detail in Fig. 4.4(c) is compared to corresponding calculated shock structure at the same time instant $\Delta t = -3.9\ \mu s$ before implosion. The computational cell size is given for reference. As seen experimental and calculated shock structures are well correlated.

The shock propagation acquired from the calculations is presented and compared to the experimental data. Very good agreement was found for the converging shock wave, while the numerical solution overestimated the velocity of the reflected wave in the outer test section. This is an indication that flow

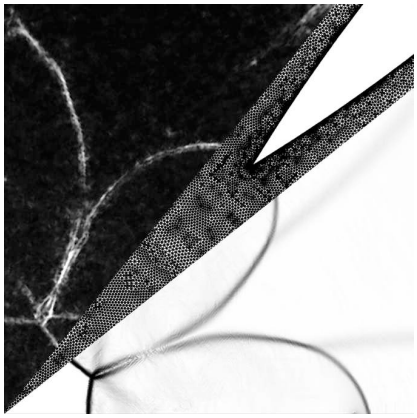

FIGURE 5.4. Comparison of a detail of a schlieren photograph Fig. 4.4(c), computational mesh and numerical schlieren image computed at the same instant $\Delta t = -3.9\ \mu s$ prior to implosion.

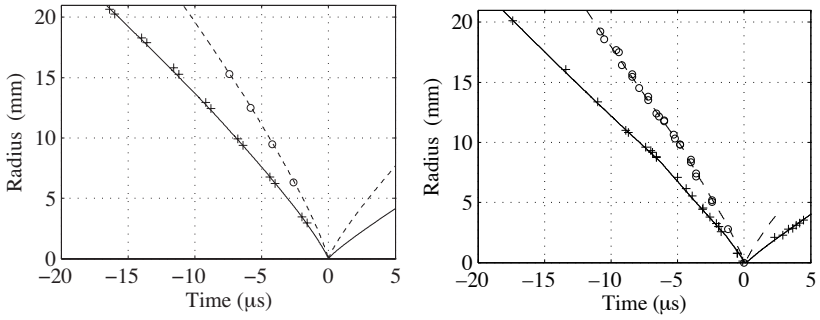

(a) (b)

FIGURE 5.5. Propagation of circular (a) and octagonal (b) shocks, comparison between Euler solver and experiments for shock waves in argon ($M_s = 3.8$, o,dashed lines) and air ($M_s = 2.4$, +,full lines).

model initial conditions does not capture the complex three-dimensional effects in the bend in the real tube. However, the numerical solution captures well the dynamics of the reflected wave right after implosion and the discrepancy is not seen until later. The numerical scheme thus solves the converging shock and the conditions behind it well until and right after implosion, but the method to initiate the flow cannot resolve the later stages of the reflected shock.

CHAPTER 6

Summary and outlook

The work focuses on studying the concentration of energy through shock wave convergence.

A major issue with achieving high energy concentrations is that of stability. Most studies show that strong circular cylindrical shock waves are unstable, loosing symmetry and focussing unevenly. Polygonal shock waves are dynamically more stable, and even though they in practice do not achieve as high energy concentrations as perfectly circular shocks the added repeatability make them suitable for study.

Large parts of the experimental work were to find an appropriate spectrometric set-up in order to measure the light emission. Several devices were tested and found insufficient due to various reasons. Eventually a compact echelle-type spectrometer able to resolve the full visible spectrum and parts of the infrared and ultraviolet regions. The spectrum of the 10 μs long light emission was measured, time-integrated and resolved into 60 ns windows. The spectrum was found to resemble a blackbody radiator with added single emission lines from excited states in argon. No ion lines have yet been found, but the excited states of the found lines are not far from the ionisation level and real gas effects must be considered when calculating. Blackbody temperatures of up to $\sim$6000 K were detected, which is considered a lower limit of the actual conditions in the gas. The radiation was collected from a comparatively large area (circular area with $r \sim 9$ mm).

Theoretical and numerical work was performed to complement the experiments and provide a ground for analysis of the experimental data. The method of characteristics to solve the shock convergence was extended to allow ionisation and departure from a perfect gas due to Coulomb forces between charged particles in the resulting plasma core. The strong effect of ionisation on the temperature close to the centre was demonstrated. The stability of the shock waves compromises a limit to how close symmetry is conserved and if the circular shock always collapses before this region is reached, real gas effects would be of academic interest only. However, experiments show that these kind of conditions are indeed reached at the focus and it is therefore necessary to make these modifications in order to predict or analyse the shock focusing process.

The dynamics of circular and polygonal shocks were experimentally studied using primarily schlieren optics. Values for the self-similarity exponent for circular and polygonal shock waves in air were determined and found to agree well with established theory. Rough values for shock waves in argon were also acquired: these may be determined more accurately by further experiments. The propagation of polygonal shock waves was quantitatively compared with geometrical shock dynamics and reasonable agreement was found also here.

6.0.2. *Future work*

6.0.2a. *Experiments.* Renewed studies of the light emissions should be made, focusing more on the spectrometric measurements and analysis. Spatially resolved spectra should preferably be taken, if the shock focus position can be kept reasonably stable. Spatial and temporal resolution of the light pulse would allow better determination of the gas conditions. Determination of the excited gas temperature and equilibrium conditions through Boltzmann plots should be made. Introduction of other gases than argon is also interesting, from the points of view of both gas dynamics and spectrometry.

A number of different interesting studies could be made on the shock dynamics, e.g.:

- Experimental determination of the power-law for gases of different γ in order to compare with theory.
- Variation of the number of sides in the polygonal shocks, to make further quantitative comparisons with the calculations made by Schwendeman & Whitham (1987).
- Convergence in a new conical end section to study 3D effects.

6.0.2b. *Numerical work.* The Euler solver can be used for calculations on the effect of ionisation on temperature and compared with experiments and the solutions acquired by shock dynamics. Especially, the temperature field acquired by the solver might be used for spectrum simulations to compare with the measured spectra. Since the temperature field is resolved in time and space by the Euler code, the error caused by capturing spectra which are time- or space-integrated can be studied in detail.

CHAPTER 7

Papers and authors contributions

Paper 1

Thermal radiation from a converging shock implosion.
M. Kjellander (MK), N. Tillmark (NT) & N. Apazidis (NA). Accepted for publication in *Phys. Fluids*.

This paper is a spectrometric and photometric study of the light emission produced by converging shock waves in argon. For repeatability purposes, polygonal shape shocks were created. The experiment was set up by MK and NT with assistance from Olli Launila and Lars-Erik Berg, KTH Applied Physics and performed by MK. Numerical calculations complemented the study, performed by NA and MK. The paper was written by MK and NA, with feedback from NT.

Paper 2

Shock dynamics of imploding spherical and cylindrical shock waves with real gas effects.
M. Kjellander, N. Tillmark & N. Apazidis.

This paper is a theoretical study on the high temperature gas processes close to the centre of convergence of cylindrical and spherical shock waves in monatomic gases. The method of characteristics was used, with a gas model accounting for ionization and Coulomb effects. The initial idea was proposed by NA and the calculations were performed mostly by MK. Theoretical derivations were made by MK and NT. The paper was written by MK with feedback from the co-authors.

Paper 3

Regular versus Mach reflection for converging polygonal shocks.
V. Eliasson (VE), M. Kjellander & N. Apazidis. *Shock Waves* **17**, 43–50.

Different reflection patters in polygonal shock waves were investigated. Square and triangular shocks were created by cylindrical rods placed in the path of the shocks. The experimental setup and work was mainly done by VE, but also by MK: MK performed the experiments with the cylinders placed at 61.5 mm from the centre. The paper was written by VE with feedback from NA.

Acknowledgements

This project has been financially supported by the Göran Gustafson Foundation and the Swedish Research Council (VR). Stiftelsen Erik Petersohns minne and the P F Lindström foundation are also acknowledged for funding participation at international conferences.

First of all, I would like to express my gratitude to my supervisors Docent Nicholas Apazidis and Dr. Nils Tillmark for their enthusiasm, encouragement, support, ideas and guidance throughout the project. Great credit goes to Göran Rådberg and Kim Karlström the toolmakers, for ideas and manufacturing of experimental equipment. I am also much obliged to Lars-Erik Berg and Olli Launila at KTH Applied Physics for the assistance and loan of spectrometers.

I want to acknowledge my office-mates Bengt, Ola and Shahab as well the rest of the staff at the Department of Mechanics, who provide a working atmosphere few places can rival - special mention goes to the grease-appreciating people: Fredrik, Olle, Muld, Heiki, Markus and others. I also want to thank Ramis and Bengt for helping me with all kinds of matters. I'm bound to have missed people who deserve to be on this page; here is a thank you for you as well.

Lastly, many grateful thanks go to my family, especially Irena and the small one, for putting up with me while writing this.

March 22 2010, Stockholm
Malte

APPENDIX A

Specific heat and speed of sound from derivatives of α

In the case of no Coulomb interactions the specific heats and equilibrium speed of sound can be rewritten in terms of derivatives of α_i, which simplifies the numerical work in some cases where these are practically already calculated.

The equilibrium spped of sound a_e,

$$a_e^2 = \left(\frac{\partial p}{\partial \rho}\right)_s = \gamma \left(\frac{\partial p}{\partial \rho}\right)_T \tag{A.1}$$

where $\gamma = c_p/c_v$. Using the enthalpy and energy, we aim to express a_e in terms of known quantities and derivatives:

$$h = \frac{5}{2}(1+\alpha_e)RT + R\sum_{i=1}^{\ell}\alpha_i \sum_{j=1}^{i}\frac{I_j}{k} \tag{A.2}$$

$$e = \frac{3}{2}(1+\alpha_e)RT + R\sum_{i=1}^{\ell}\alpha_i \sum_{j=1}^{i}\frac{I_j}{k} \tag{A.3}$$

$$c_p = \left(\frac{\partial h}{\partial T}\right)_p = \frac{5}{2}(1+\alpha_e)R + \frac{5}{2}TR\left(\frac{\partial \alpha_e}{\partial T}\right)_p + R\sum_{i=1}^{\ell}\left(\frac{\partial \alpha_i}{\partial T}\right)_p \sum_{j=1}^{i}\frac{I_j}{k} \tag{A.4}$$

$$c_v = \left(\frac{\partial e}{\partial T}\right)_v = \frac{3}{2}(1+\alpha_e)R + \frac{3}{2}TR\left(\frac{\partial \alpha_e}{\partial T}\right)_v + R\sum_{i=1}^{\ell}\left(\frac{\partial \alpha_i}{\partial T}\right)_v \sum_{j=1}^{i}\frac{I_j}{k} \tag{A.5}$$

where

$$\left(\frac{\partial \alpha_e}{\partial T}\right)_F = \sum_{i=1}^{\ell}\left(\frac{\partial \alpha_i}{\partial T}\right)_F \tag{A.6}$$

Using the equation of state, Eq. 2.11,

$$a_e^2 = \gamma\left(\frac{\partial p}{\partial \rho}\right)_T = \frac{c_p}{c_v}\left(\frac{\partial p}{\partial \rho}\right)_T = \frac{c_p}{c_v}\frac{\partial}{\partial \rho}\Big(\rho(1+\alpha_e)RT\Big)_T = \frac{c_p}{c_v}\left[(1+\alpha_e)RT + \rho RT\left(\frac{\partial \alpha_e}{\partial \rho}\right)_T\right] \tag{A.7}$$

The above expression together with A.4 and A.5 is used to calculate a_e. All thermodynamic variables are known but the derivatives of α_i has to be evaluated numerically around the current state of the gas p, ρ, T, α_i. A simple evaluation is employed,

$$\left(\frac{\partial \alpha_i}{\partial F}\right)_G = \frac{\alpha_i(F + dF_1, G) - \alpha_i(F - dF_2, G)}{dF_1 + dF_2} \tag{A.8}$$

APPENDIX B

Coulomb effects on thermodynamic variables

In a partly ionised gas Coulomb forces between the charged particles lead to departures from the ideal state. When the effect is weak, consideration to the Coulomb interactions may be taken in form of correction terms to the thermodynamic variables. Different models exist for different gas conditions: here is a derivation using the Debye-Hückel model for the ion charges for weak Coulomb interactions. To derive the corrections due to the Coulomb forces on the thermodynamic state and the species distribution, the electrostatic energy contribution to the free energy is found, which in turn gives the desired corrections. The electrostatic potential around a point charge is found by considering the other particles not as individual charges but as a uniform charge cloud and solving the Poisson equation. The derivation of the potential may be found in e.g. Griem (1962), Ebeling (1976) or Salzmann (1998). The electrostatic energy of a gas in a volume V resulting from this first approximation is given as:

$$E_c = -\frac{kTV}{8\pi r_D^3} \tag{B.1}$$

The parameter r_D is the Debye radius which is a characteristic of the surrounding charge cloud and determines the sphere of influence of the ion charge, which for a single-temperature plasma may be written:

$$r_D = \left[\frac{q^2}{\epsilon_0 kT}(n_e + \sum_i^{\ell} n_i z_i^2)\right]^{-1/2} = \left[\frac{q^2}{\epsilon_0 kTV}(N_e + \sum_i^{\ell} N_i z_i^2)\right]^{-1/2} \tag{B.2}$$

where q is the elementary charge, ϵ_0 is the vacuum permittivity, $z_i{=}i$ is the charge state of the ion i. Note that several of the cited authors have used other unit systems, while SI units are used here. The number particles of different species N_j in the volume V and number densities $n_j = N_j/V$ are defined as usual. Outside the Debye sphere, which is the sphere around the ion with a radius r_D, the ion is effectively screened by the cloud. A typical validity requirement for the statistical Debye-Hückel model is that several ions must be present within a Debye sphere.

The influence of the Coulomb forces on the free energy is expressed as a correction term to the ideal gas energy, $F = F_{ig} + F_C$, which derives from the electrostatic energy. Using $E = -T^2\partial/\partial T(F/T)$, the correction to the free energy becomes:

$$F_C = -\frac{kTV}{12\pi r_D^3} \tag{B.3}$$

B.0.3. *Equation of state*

The pressure follows from the free energy as $p = (\partial F/\partial V)_{N_i,T}$. The ideal translational contribution to the pressure is given in Eq. 2.11. The correction term is then found from Eq. B.3 as:

$$\delta p_C = -\left(\frac{\partial F_C}{\partial V}\right)_{N_i,T} = \frac{kT}{12\pi r_D^3} - \frac{kTV}{12\pi r_D^3}\frac{3}{2V} = -\frac{kT}{24\pi r_D^3} \tag{B.4}$$

For completeness, the total pressure including the Coulomb correction is then written:

$$p = p_{ig} + p_C = \rho(1+\alpha_e)RT + \delta p_C \tag{B.5}$$

B.0.4. *Saha equation*

The Saha equation may be derived from minimising the free energy considering the ionisation reaction where the $(i+1)$th electron is removed from the atomic species A:

$$A_i \rightleftharpoons A_{i+1} + e^-, \quad i = 0, 1, 2, \ldots \ell\text{–}1 \tag{B.6}$$

where ℓ denotes the atomic number of A. The free energy of the ideal gas F_{ig} is given by statistical mechanics. With the Coulombic correction the free energy of a partially ionised gas in local thermodynamic equilibrium becomes:

$$F = F_{ig} + F_C = -\sum_{i=1}^{\ell} N_i kT \ln\frac{Z_i e}{N_i} - N_e kT \ln\frac{Z_e e}{N_e} + F_C \tag{B.7}$$

where Z_i and Z_e are the partition functions of the ions and free electrons. Differentiating and setting $(\delta F)_{V,T} = 0$:

$$\delta F = \sum_j \frac{\partial(F_{ig} + F_c)}{\partial N_j}\delta N_j = \sum_j \left(\frac{\partial F_{ig}}{\partial N_j} + \mu_{j,C}\right)\delta N_j = 0 \tag{B.8}$$

where $\mu_{C,j} = \partial F_C/\partial N_j$ and the summation j is for $j = i$, $j = i+1$ and $j = e$. According to the reaction in Eq. B.6 $\delta N_i = -\delta N_{i+1} = -\delta N_e$ and Eq. B.8 becomes:

$$\left(\frac{\partial F_{ig}}{\partial N_i} - \frac{\partial F_{ig}}{\partial N_{i+1}} - \frac{\partial F_{ig}}{\partial N_e} + \mu_{C,i} - \mu_{C,i+i} - \mu_{C,e}\right)\delta N_i = 0 \;\rightarrow$$
$$-kT\ln\frac{Z_i e}{N_i} + N_i kT\frac{1}{N_i} + \mu_{C,i} +$$
$$-(-kT\ln\frac{Z_{i+1}e}{N_{i+1}} + N_{i+1}kT\frac{1}{N_{i+1}} + \mu_{C,i+i}) +$$
$$-(-kT\ln\frac{Z_e e}{N_e} + N_e kT\frac{1}{N_e} + \mu_{C,e}) = 0 \;\rightarrow$$

$$\ln\left(\frac{Z_{i+1}Z_e e N_i}{N_{i+1}N_e Z_i}\right) - 1 = -\frac{\mu_{C,i} - \mu_{C,i+i} - \mu_{C,e}}{kT} \tag{B.9}$$

Defining the reduction in ionisation potential due to the Coulomb interactions as:

$$\Delta I_{i+1} \equiv \mu_{C,i} - \mu_{C,i+i} - \mu_{C,e} \tag{B.10}$$

Eq. B.9 becomes:

$$\frac{N_{i+1}N_e}{N_i} = \frac{Z_{i+1}Z_e}{Z_i}\exp\left(\frac{\Delta I_{i+1}}{kT}\right) \tag{B.11}$$

This can be written in terms of the particles densities n_j by dividing with the volume V and using that $N_j = n_j V$:

$$\frac{n_{i+1}n_e}{n_i} = \frac{1}{V}\frac{Z_{i+1}Z_e}{Z_i}\exp\left(\frac{\Delta I_{i+1}}{kT}\right) \tag{B.12}$$

The partition functions for a monatomic ion consist of one translational and one internal part, $Z_i = Z_i^{tr} Z_i^{el}$, the latter accounting for the excited electrons within the ion. The translational contributions is:

$$Z_i^{tr} = V\left(\frac{2\pi m_i kT}{h^2}\right)^{3/2} \tag{B.13}$$

where m_i is the molecular weight of the i:th ion, k the Boltzmann constant and h the Planck constant. Since the weight difference of the successive ions are negligible, the translational part of the partition functions cancel in Eq. B.11 and B.11. The electronic contribution can be rewritten (Zel'dovich & Raizer (2002)):

$$Z_i^{el} = \sum_l e^{-\varepsilon_{l,i}/kT} = e^{-\varepsilon_{0,i}/kT}\sum_l e^{-(\varepsilon_{l,i}-\varepsilon_{0,i})/kT} = e^{-\varepsilon_{0,i}/kT}Q_i^{el} \tag{B.14}$$

where ε_0 is the ground state of ion i and the summation is taken over all energy states. In other words, the transformed partition function Q^{el} relates the energy of each electronic level to the ground state of the individual ions instead

of to the ground state of the atom. The energy differences of the succesive ionic ground states are equal to the ionisation potentials, $\varepsilon_{0,i+1} - \varepsilon_{0,i} = I_{i+1}$.

The partition function of the free electrons has one temperature-dependent contribution from the translational energy and one constant contribution related to the spin, $Z^{spin} = 2$. The total electron partition function is then:

$$Z_e = 2V \left(\frac{2\pi m_e kT}{h^2} \right)^{3/2} \tag{B.15}$$

where m_e is the electron weight. Inserting Eq:s B.13, B.14 and B.15 into Eq. B.12 yields the Saha equation:

$$\frac{n_{i+1} n_e}{n_i} = 2 \left(\frac{2\pi m_e kT}{h^2} \right)^{3/2} \frac{Q_{i+1}^{el}}{Q_i^{el}} \exp\left(-\frac{I_{i+1} - \Delta I_{i+1}}{kT} \right) \tag{B.16}$$

Using the particle fractions $\alpha_i = n_i/n_H$ and $\alpha_e = n_e/n_H$ this is rewritten as:

$$\frac{\alpha_{i+1}\alpha_e}{\alpha_i} = \frac{2}{n_H} \left(\frac{2\pi m_e kT}{h^2} \right)^{3/2} \frac{Q_{i+1}^{el}}{Q_i^{el}} \exp\left(-\frac{I_{i+1} - \Delta I_{i+1}}{kT} \right) \tag{B.17}$$

Noting that $\rho \approx n_H m_H$, Eq. B.17 has the same form as Eq. 5.19. The equation of state B.5 can be used to rewrite the equation as a function of temperature and pressure:

$$\frac{\alpha_{i+1}}{\alpha_i} = \frac{1 + \alpha_e}{\alpha_e} \left(\frac{2\pi m_e}{h^2} \right)^{3/2} \frac{(kT)^{5/2}}{p - \delta p_C} \frac{2Q_{i+1}^{el}}{Q_i^{el}} \exp\left(-\frac{I_{i+1} - \Delta I_{i+1}}{kT} \right) \tag{B.18}$$

The potential reduction according to the Debye-Hückel method is received by taking the derivative of Eq. B.3:

$$\Delta I_{i+1} = \frac{\partial F_C}{\partial N_i} - \frac{\partial F_C}{\partial N_{i+1}} - \frac{\partial F_C}{\partial N_e} = \frac{(i+1)q^2}{4\pi\epsilon_0 r_D} \tag{B.19}$$

B.0.5. *Energy equation*

The expression for the energy may be calculated from $E = -T^2 \partial/\partial T(F/T)$ using the partition functions. Again $F = F_{ig} + F_C$, with F_{ig} for a partially ionised monatomic gas in local thermodynamic equilibrium given in Eq. B.7. The Coulombic correction from the elecrostatic potential is given in Eq. B.1. Dividing the partition functions in their translational and electronic parts, $Z = Z^{tr} Z^{el}$ yields:

$$\left(\frac{\partial}{\partial T}\frac{F_{ig}}{T}\right)_{V,N} = -k\sum_{i=0}^{\ell}\left[N_i\left(\frac{\partial \ln Z_i^{tr}}{\partial T}\right)_{V,N} + N_i\left(\frac{\partial \ln Z_i^{el}}{\partial T}\right)_{V,N}\right] - kN_e\left(\frac{\partial \ln Z_e^{tr}}{\partial T}\right)_{V,N}$$
$$= -k\sum_{i=0}^{\ell}\left[N_i\frac{3}{2}\frac{1}{T} + N_i\left(\frac{\partial \ln Z_i^{el}}{\partial T}\right)_{V,N}\right] - kN_e\frac{3}{2}\frac{1}{T} \quad \text{(B.20)}$$

The total number of heavy particles, $N_0 = \sum_{i=0}^{\ell} N_i$:

$$E_{ig} = -T^2\left(\frac{\partial}{\partial T}\frac{F_{ig}}{T}\right)_{V,N} = \frac{3}{2}(N_0+N_e)kT + kT^2\sum_{i=0}^{\ell}N_i\left(\frac{\partial \ln Z_i^{el}}{\partial T}\right)_{V,N} =$$
$$= \frac{3}{2}(1+\alpha_e)N_0kT + kT^2N_0\sum_{i=0}^{\ell}\alpha_i\left(\frac{\partial \ln Z_i^{el}}{\partial T}\right)_{V,N} \quad \text{(B.21)}$$

The last term is rewitten using Eq. B.14:

$$\sum_{i=0}^{\ell}\alpha_i\left(\frac{\partial \ln Z_i^{el}}{\partial T}\right)_{V,N} = \sum_{i=0}^{\ell}\alpha_i\left(\frac{\partial \ln Q_i^{el}}{\partial T}\right)_{V,N} + \sum_{i=0}^{\ell}\alpha_i\left(\frac{\partial \ln e^{-\varepsilon_{0,i}/kT}}{\partial T}\right)_{V,N} =$$
$$= \sum_{i=0}^{\ell}\alpha_i\left(\frac{\partial \ln Q_i^{el}}{\partial T}\right)_{V,N} + \sum_{i=1}^{\ell}\alpha_i\sum_{j=1}^{i}\frac{I_j}{kT^2} \quad \text{(B.22)}$$

Using that the masses of the ionic species is approximately equal to the atomic mass $M_i \approx M_A \rightarrow N_0k \approx mR_A$ and the energy is rewritten:

$$E_{ig} = \frac{3}{2}(1+\alpha_e)mR_AT + mR_A\sum_{i=1}^{\ell}\alpha_i\sum_{j=1}^{i}\frac{I_j}{k} + mR_AT^2\sum_{i=0}^{\ell}\alpha_i\left(\frac{\partial \ln Q_i^{el}}{\partial T}\right)_{V,N} \quad \text{(B.23)}$$

The enthalpy per unit mass $h = e + p/\rho$ is similarily divided into an ideal and Coulombic part: $h = e_{ig} + e_C + (p_{ig} + p_C)/\rho$. The ideal enthalpy is acquired directly from Eq. B.5 and Eq. B.23:

$$h_{ig} = \frac{5}{2}(1+\alpha_e)R_AT + R_A\sum_{i=1}^{\ell}\alpha_i\sum_{j=1}^{i}\frac{I_j}{k} + R_A\sum_{i=0}^{\ell}\alpha_iW_i \quad \text{(B.24)}$$

where the energy of the electronic excitation is:

$$W_i = T^2\left(\frac{\partial \ln Q_i^{el}}{\partial T}\right)_{V,N} \quad \text{(B.25)}$$

The enthalpy have two Coulomb corrections, which are acquired from Eq:s B.1 and B.4:

$$h_C = e_C + p_C/\rho = \frac{1}{\rho V}E_C + p_C/\rho = -\frac{kT}{8\pi\rho r_D^3} - \frac{kT}{24\pi\rho r_D^3} = -\frac{kT}{6\pi\rho r_D^3} \quad \text{(B.26)}$$

References

Anderson, J. 2003 *Modern Compressible Flow*, 3rd edn. McGraw-Hill, New York.

Apazidis, N. & Lesser, M. 1996 On generation and convergence of polygonal-shaped shock waves. *J. Fluid Mech.* **309**, 301–319.

Apazidis, N., Lesser, M., Tillmark, N. & Johansson, B. 2002 An experimental and theoretical study of converging polygonal shock waves. *Shock waves* **12**, 39–58.

Aslan, N. & Mond, M. 2005 A numerical scheme for ionizing shock waves. *J. Comput. Phys.* **210**, 410–420.

Ben-Dor, G. 2007 *Shock Wave Reflection Phenomena*, 2nd edn. Springer-Verlag, Berlin.

Ben-Dor, G. & Takayama, K. 1992 The phenomena of shock wave reflection - a review of unsolved problems and future research needs. *Shock Waves* **2**, 211–223.

Butler, D. 1954 *Converging spherical and cylindrical shocks, Report No. 54/54*. Burgess Hill, New York.

Chester, W. 1954 The quasi-cylindrical shock tube. *Phil. Mag.* **45**, 1293–1301.

Chisnell, R. 1955 The normal motion of a shock wave through a nonuniform one-dimensional medium. *Proc. R. Soc. London* **232**, 350–370.

Chisnell, R. 1998 An analytic description of converging shock waves. *J. Fluid Mech.* **354**, 357–375.

de Neef, T. & Hechtman, C. 1978 Numerical study of the low due to cylindrical implosion. *Computers and Fluids* **6**, 185–202.

Ebeling, W. 1976 *Theory of bound states and ionization equilibrium in plasmas and solids*. Akademie-Verlag, Berlin.

Eliasson, V. 2007 On focusing of shock waves. PhD thesis, KTH, Stockholm, TRITA-MEK Tech. Rep. 2007:06.

Eliasson, V., Apazidis, N. & Tillmark, N. 2007*a* Controlling the form of strong converging shocks by means of disturbances. *Shock Waves* **17**, 29–42.

Eliasson, V., Apazidis, N., Tillmark, N. & Lesser, M. B. 2006 Focusing of strong shocks in an annular shock tube. *Shock Waves* **15**, 205–217.

Eliasson, V., Tillmark, N., Szeri, A. & Apazidis, N. 2007*b* Light emission during shock wave focusing in air and argon. *Phys. Fluids* **19**, 106106.

Emrich, R. & Wheeler, D. 1958 Wall effects in shock tube flow. *Phys. Fluids* **1**, 14–23.

Fujimoto, Y. & Mishkin, E. 1978 Analysis of spherically imploding shocks. *Phys. Fluids* **21**, 1933–1938.

Glass, I. & Sharma, S. 1976 Production of diamonds from graphite using explosive-driven implosions. *AIAA J.* **14**, 402–404.

Griem, H. R. 1962 High density corrections in plasma spectroscopy. *Phys. Rev.* **128**, 997–1003.

Guderley, G. 1942 Starke kugelige und zylindrische Verdichtungsstöße in der Nähe des Kugelmittelpunktes bzw. der Zylinderachse. *Luftfahrtforschung* **19**, 302–313.

Hafner, P. 1988 Strong convergent shock waves near the center of convergence: A power series solution. *J. Appl. Math.*. **48**, 1244–1261.

Henshaw, W., Smyth, N. & Schwendeman, D. 1986 Numerical shock propagation using geometrical shock dynamics. *J. Fluid Mech.* **171**, 519–545.

Hornung, H. G. 1986 Regular and mach reflections of shock waves. *Ann. Rev. Fluid Mech.* **18**, 33–58.

Hornung, H. G., Pullin, D. I. & Ponchaut, N. 2008 On the question of universality of imploding shock waves. *Acta Mech.* **201**, 31–35.

Hosseini, S. H. R. & Takayama, K. 2005 Implosion from a spherical shock wave reflected from a spherical wall. *J. Fluid Mech.* **530**, 223–239.

Johansson, B. 2000 *Experimental study of shock wave focusing in a confined reflector*. Lic. Thesis: Royal Institute of Technology, Stockholm, Sweden.

Johansson, B., Apazidis, N. & Lesser, M. 1999 On shock waves in a confined reflector. *Wear* **233-235**, 79–85.

Kleine, H. 1985 Time resolved shadowgraphs of focusing cylindrical shock waves. *Tech. Rep.*. RWTH, Aachen, Germany.

Knystautas, R., Lee, B. & Lee, J. 1969 Diagnostic Experiments on Converging Detonations. *Phys. Fluids Suppl.* **12**, I–165.

Lazarus, R. 1980 Comments on "Analysis of spherical imploding shocks". *Phys. Fluids* **23**, 844.

Lazarus, R. & Richtmyer, R. 1977 *Similarity Solutions for Converging Shocks*. Los Alamos Scientific Laboratory of the University of California, Los Alamos, NM.

Lee, J. & Knystautas, R. 1971 Experiments on the Stability of Converging Cylindrical Detonation. *Combust. Flame* **16**, 61.

Matsuo, H., Ebihara, K. & Ohya, Y. 1985 Spectroscopic study of cylindrically converging shock waves. *J. Appl. Phys.* **58**, 2487–2491.

Michaut, C., Stehl, C., Leygnac, S., Lanz, T. & Boireau, L. 2004 Jump conditions in hypersonic shocks. *Eur. Phys. J. D* **28**, 381–392.

Mishkin, E. & Fujimoto, Y. 1978 Analysis of a cylindrical imploding shock wave. *J. Fluid Mech.* **89**, 61–78.

Nakamura, Y. 1983 Analysis of self-similar problems of imploding shock waves by the method of characteristics. *Phys. Fluids* **26**, 1234–1239.

Neemeh, R. & Ahmad, Z. 1986 Stability and collapsing mechanism of strong and weak converging cylindrical shock waves subjected to external perturbation. In

Shock waves and shock tubes; Proc. 15th Intern. Symp., pp. 107–114. Stanford, CA: Stanford University Press.

Nieuwenhuijzen, H., de Jager, C., Cuntz, M., Lobel, A. & Achmad, L. 1992 A generalized version of the rankine-hugoniot relations including ionization, dissociation, radiation and related phenomena. *Astron. Astrophys,* **28**, 195–200.

NIST 2008 Atomic spectra database, version 3.0.

Perry, R. W. & Kantrowitz, A. 1951 The production and stability of converging shock waves. *J. Appl. Phys* **22**, 878–886.

Ponchaut, N., Hornung, H. G. & Mouton, D. I. 2006 On imploding cylindrical and spherical shock waves in a perfect gas. *J. Fluid. Mech.* **560**, 102–122.

Resler, E., Lin, S.-C. & Kantrowitz, A. 1952 The production of high temperatures in shock tubes. *J. App. Phys.* **23**, 1390–1399.

Roberts, D. & Glass, I. 1971 Spectroscopic investigation of combustion-driven spherical implosion waves. *Phys. Fluids* **14**, 1662–1670.

Roig, R. & Glass, I. 1977 Spectroscopic study of combustion-driven implosions. *Phys. Fluids* **20**, 1651–1656.

Saito, T. & Glass, I. 1982 Temperature Measurements at an Implosion Focus. *Proc. R. Soc. Lon. A* **384**, 217–231.

Salzmann, D. 1998 *Atomic Physics in Hot Plasmas*. Oxford University Press, New York.

Schwendeman, D. W. & Whitham, G. B. 1987 On Converging Shock Waves. *Proc. R. Soc. Lon. A* **413**, 297–311.

Stanyukovich, K. 1960 *Unsteady motion of continous media*. Pergamon, Oxford.

Sun, M. & Takayama, K. 2003 An artificially upstream flux vector splitting scheme for the Euler equations. *J. Comput. Phys.* **189**, 305–329.

Takayama, K., Kleine, H. & Grönig, H. 1987 An experimental investigation of the stability of converging cylindrical shock waves in air. *Exps. Fluids* **5**, 315–322.

Trayner, C. & Glowacki, M. 1995 A new technique for the solution of the saha equation. *J. Sci. Comput.* **10**, 139–149.

Van Dyke, M. & Guttman, A. 1982 The converging shock wave from a spherical or cylindrical piston. *J. Fluid Mech.* **120**, 451–462.

Watanabe, M., Onodera, O. & Takayama, K. 1995 Shock wave focusing in a vertical annular shock tube. In *Proc. 19th Intern. Symp. on Shock Waves* (ed. R. Brun & L. Dimitrescu), pp. 61–79. Springer-Verlag, Berlin.

Watanabe, M. & Takayama, K. 1991 Stability of converging cylindrical shock waves. *Shock Waves* **1**, 149–160.

Welsh, R. 1967 Imploding shocks and detonations. *J. Fluid Mech,* .

Whitham, G. 1958 On the propagation of shock waves through regions of non-uniform area or flow. *J. Fluid Mech.* **4**, 337–360.

Whitham, G. 1973 *Linear and nonlinear waves*. John Wiley and Sons, New York.

Zel'dovich, Y. B. & Raizer, Y. P. 2002 *Physics of Shock Waves and High-Temperature Hydrodynamic Phenoma*. Mineola, New York.